Energy Absorption and Dynamic Behaviors of Architectured Interpenetrating Phase Composites

by

Spencer V. Taylor

B.S. Materials Science and Engineering
University of North Texas, 2019

Submitted to the Department of Aeronautics and Astronautics
in partial fulfillment of the requirements for the degree of

Master of Science in Aerospace Engineering

at the

MASSACHUSETTS INSTITUTE OF TECHNOLOGY

May 2022

Author .....
Department of Aeronautics and Astronautics
May 17, 2022

Certified by .....
Zachary C. Cordero
Boeing Assistant Professor of Aeronautics and Astronautics
Thesis Supervisor

Accepted by .....
Jonathan P. How
R. C. Maclaurin Professor of Aeronautics and Astronautics Chair,
Graduate Program Committee

Energy Absorption and Dynamic Behaviors of Architectured Interpenetrating Phase Composites

by

Spencer V. Taylor

Submitted to the Department of Aeronautics and Astronautics
on May 17, 2022, in partial fulfillment of the
requirements for the degree of
Master of Science in Aerospace Engineering

Abstract

Novel interpenetrating phase composites show promise for structural aerospace components, but their structure-property relations are not well understood. In this work, we explore the effects of mesoscale geometry on mechanical behaviors of architectured interpenetrating phase composites. We first investigate the tensile behavior of a composite construction termed the chain lattice, which is a hierarchical porous structure comprising two interpenetrating cellular solids. Through tension testing, we demonstrate that combined interphase action results in damage delocalization and an order-of-magnitude improvement in strain-to-failure over the fully dense base material. These experiments validate a micromechanics-based model of tensile specific energy absorption, which we then use in a parametric study on the effects of geometric parameters and matrix properties on tensile behavior. We predict that ceramic chain lattices can achieve an order-of-magnitude improvement in tensile specific energy absorption over the fully dense material. We next examine the macroscale and fine-scale dynamic response of interpenetrating phase composites comprising a body-centered cubic steel lattice embedded in an aluminum matrix. Through plate impact simulations, we find that the complex mesoscale geometry reduces shock velocity relative to monolithic constituents, slowing and spreading the shock front via reflection and redirection. In the fine-scale, we can predict several aspects of the pressure and longitudinal velocity responses by tracking internal wave reflections. Finally, we observe that the post-shock maximum temperature increases with structural openness, and temperature hotspots form at interfaces parallel to the shock direction. The findings in this work 1) highlight the ability to tailor energy absorption of interpenetrating phase composites by controlling mesoscale geometry; and 2) provide novel structure-property linkages in the dynamic response of architectured interpenetrating phase composites.

Thesis Supervisor: Zachary C. Cordero
Title: Boeing Assistant Professor of Aeronautics and Astronautics

Acknowledgments

First, I would like to thank my advisor, Professor Zachary Cordero, for his continuous drive and inspiration. I am incredibly lucky to be at MIT, where I get to work with Zack and the members of the Cordero Lab who offer unending kindness and support.

Next, I would like to thank our collaborators whose expertise helped advance this work. Thank you to Dr. Abdel Moustafa for giving direction to the chain lattice project and for guiding me as a first-year graduate student at Rice University. Thank you to Dr. Manny Gonzales, Austin Gerlt, Lauren Poole, and Dr. Peter Sable for laying the foundation for the shock dynamics studies, for passing along valuable shock dynamics knowledge, and for troubleshooting my CTH simulations. And thank you to Dr. Bernard Gaskey and Dr. Philip Flater for your scientific discussion and support.

I gratefully acknowledge support from the National Defense Science and Engineering Graduate (NDSEG) Fellowship; and I thank my NDSEG mentor, Dr. David Mollenhauer, who is always willing to give his perspective on science and on life.

Finally, I would like to acknowledge those close to me personally. Thank you to my friends and former colleagues at Rice University; to my peers in the AeroAstro department and those who come out to play intramural sports; and to my family and my girlfriend, Nancy.

Contents

1 Introduction **13**

2 Background **16**

2.1 Introduction 16

2.2 Energy Absorption Behavior of Traditional Material Systems 17

2.3 Shock Behavior of Composites and Preliminary Work 19

2.4 Summary 23

3 Tensile Energy Absorption Behavior of Additively Manufactured Interpenetrating Porous Composites **25**

3.1 Introduction 25

3.2 Analytical Model for Energy Absorption 27

3.3 Experimental Validation 30

3.3.1 Procedure 30

3.3.2 Results and Discussion 32

3.4 Parametric Analysis of Energy Absorption 38

3.5 Summary 40

4 Shock Response of Additively Manufactured Interpenetrating Phase Composites **42**

4.1 Introduction 42

4.2 Plate Impact Simulation Setup 43

4.3 Macroscale Composite Shock Properties 44

4.4 Fine-Scale Shock Response 52
4.4.1 Oscillatory Behavior 52
4.4.2 Orientation Dependence 64
4.5 Summary 69

5 Conclusions and Future Work **70**

List of Figures

2-1 Pressure response of laminated composites with layers (a) perpendicular, (b) angled, and (c) parallel to the impact direction [38]. 20

2-2 Schematic representation of the PrintCast process used to form metal interpenetrating phase composites. 22

2-3 Tensile stress-strain curves for monolithic A356 Al and a BCC steel-Al IPC. From [13]. 23

2-4 Shock front behavior in a 2-D cross-section of a BCC steel-Al IPC. From [46]. 24

3-1 Chain lattice comprising a unidirectional chain reinforcement embedded in a random foam of the same base material. Key features of the racetrack chain links (thickness T, length L, crown radius R) are labeled in the magnified view of the half-unit cell. 26

3-2 Exemplar chain lattice used for tension testing, where the individual chains are arranged in a 3×3 array embedded within the filler matrix. 31

3-3 (a) Compressive stress-strain data and (b) compressive strength vs. relative density for 3-D-printed poly(methyl methacrylate) filler foams with varying relative densities. 32

3-4 Tensile stress-strain data for 3-D-printed poly(methyl methacrylate) as a fully dense material and as filler foams with varying relative density $\bar{\rho}$. 33

3-5 Tensile stress-strain data for 3-D-printed poly(methyl methacrylate) chain lattices with overall relative density $\tilde{\rho}$ ranging from 0.25 to 0.58 and filler relative density $\bar{\rho}$ (in parentheses) ranging from 0.13 to 0.28. 34

3-6 Plastic Poisson's ratio $\nu_{plastic}$ vs. relative density $\bar{\rho}$ for poly(methyl methacrylate) foams in compression. 36
3-7 Specific energy absorption of chain lattices, compressive foams, tensile foams, and fully dense poly(methyl methacrylate). For the chain lattices, overall relative densities $\tilde{\rho}$ are followed by filler relative densities $\bar{\rho}$ in parentheses. 37
3-8 Normalized specific energy absorption Φ vs. relative density $\bar{\rho}$ for chain lattices with (a) bend-dominated and (b) stretch-dominated filler matrices, with $\frac{L}{T} = 3$, $m = 10$, and selected values of $\frac{R}{T}$. 39
3-9 Contours of delocalized damage threshold $\bar{\rho}$ with variation in geometric parameters $\frac{R}{T}$ and $\frac{L}{T}$. 40
3-10 Normalized specific energy absorption Ψ for chain lattices with (a) bend-dominated and (b) stretch-dominated filler matrices. 41

4-1 (a) Simulation setup and (b) variations in impact orientation and lattice volume fraction. 44
4-2 (a) Simulated composite Hugoniot relation compared to experimental Hugoniot relations of the constituent materials and a kinetic energy average prediction, with points from the simulated [110] and [111] impact orientations overlaid, and (b) simulated composite shock speed with varying lattice volume fraction. 45
4-3 Schematic comparison of the structural openness within laminated composites [6], 2-D cross-sections of BCC IPCs [46], and 3-D IPCs, where open channels are represented in green. 46
4-4 Pressure histories for tracer points and the plane average within a plane 3.2 mm into the composite with impact orientation of [100], impact velocity of 1000 m/s, and lattice volume fraction of 40%. 47
4-5 Contour of the shock front in the first unit cell from the strike face after 5 ns, 180 ns, and 400 ns. 49

4-6 Transverse velocity, V_T, normalized by longitudinal velocity, V_L, at given times, with vectors overlaid to indicate shock velocity (top view). Shock parameters are the following: impact direction of [100], impact velocity of 1000 m/s, and lattice volume fraction of 40%. 50
4-7 Pressure histories of 3 planes of tracer points taken from the same location within different unit cells. 51
4-8 Plane-average pressure histories from the planes in Fig. 4-7 overlaid. . 52
4-9 a) Pressure history for the tracer point located at the central node of the BCC unit cell for a lattice volume fraction of 40% and 20%, with the predicted and observed periods listed. b) Schematic depiction of the location of the tracer point at the central node of the BCC unit cell and the path of the pressure wave along the unit cell diagonal. . . 53
4-10 Graphical impedance matching for the copper projectile and the 316L stainless steel target based on Eq. 4.4, using shock parameters listed in table 4.1 and an impact velocity of 1 km/s. 54
4-11 a) Pressure history for the tracer point located at the central node of the BCC unit cell for a lattice volume fraction of 40%. b) Fourier transform of the plot in Fig. 4-11a which reveals the mean pressure σ_{mean}. 57
4-12 Pressure contour plot for 5 different time steps, showing the path of the pressure wave that results in an oscillatory pressure response measured from the tracer point shown. 59
4-13 Longitudinal displacement history at a given tracer point for varying lattice volume fraction. 60
4-14 a) Pressure history for the tracer point located at the central node of the BCC unit cell for a lattice volume fraction of 80% and 60%, with the predicted and observed periods listed. b) Schematic depiction of the location of the tracer point at the central node of the BCC unit cell and the path of the pressure wave within the steel lattice strut. . 61

4-15 (a) Longitudinal velocity history with lattice volume fraction of 40% (with 80% and 20% inset). Predicted and observed oscillation period are listed. (b) Representation of the shock wave reflection history at the given tracer point location. 63
4-16 Longitudinal velocity history with varying impact orientation. 65
4-17 Pressure histories for tracer points at a given plane in the (a) [110] and (b) [111] impact orientations, with plane averages overlaid. 67
4-18 Temperature at the shock front for the [100], [110], and [111] orientations, measured from a given plane in the center of the unit cell. Steel and Al interfaces are outlined in black. 68

5-1 Open-faced infiltrated BCC preform. 74

List of Tables

4.1 Shock parameters for copper, 316L stainless steel, and A356 aluminum. 54

4.2 Parameters used to approximate the IPCs of varying lattice volume fractions as laminated composites, and the resulting predicted vs. observed V_L period. 64

Chapter 1

Introduction

Propulsion systems and thermal protection systems in next-generation aerospace vehicles require materials that can survive extreme operating conditions such as high stresses, elevated temperatures, and aggressive oxidation. Because monolithic materials are often unable to withstand such extreme operating conditions, people have historically turned to composites for use in these extreme aerospace environments, where the composite effect grants mechanical properties that exceed those of their constituent materials. For instance, ceramic-matrix composites are attractive candidates for reusable rocket nozzles and combustion liners owing to their excellent high-temperature strength and damage tolerance [1, 2].

Structural aerospace components also frequently experience high-rate loading events. For instance, jet engine turbine blades are frequently damaged by high-speed collisions with solid particles entrained within the air such as ice particles and sand [3, 4]. Satellites and spacecraft also suffer hypersonic damage by impact of micrometeoroids and orbital debris, which travel at speeds in excess of several kilometers per second [5]. In these dynamic loading conditions, traditional laminated composites and granular compacts exhibit strong resistance to shock due to their internal geometric features which impede shock propagation [6, 7]. This unique combination of material properties—exceptional high-temperature damage tolerance and resistance to high-rate deformation—makes composites key candidates for aerospace components.

However, traditional composite processing routes present challenges which de-

grade mechanical performance relative to theoretical upper bounds. Porosity and structural heterogeneities can act as stress concentration sites, for instance, leading to premature failure [8]. Additive manufacturing (AM) offers a potential solution to this problem, since it can be used to fabricate high quality, complex structures with well-controlled geometries that impart specific, desirable failure behaviors. For example, AM has been used to precisely arrange the spatial distribution of constituents in interpenetrating phase composites (IPCs) [9, 10], which enables desirable failure mechanisms such as tailored crack bridging and damage delocalization [11, 12, 13]. Additionally, by patterning porosity in a single material, AM has been used to form interpenetrating lattices which extend the range of available mechanical properties beyond those of conventional lattice structures [14].

The ability to manipulate the mechanical behavior of 3-D-printable composite structures via the fine control of their mesoscale geometry has far-reaching implications for aerospace materials. For instance, 3-D-printable IPCs can be used to form regenerative cooling channels in rocket engines by incorporating foams and lattice structures with finely tuned porosity. They are also of interest for shock focusing in munitions casings, where hotspot formation within reactive IPC systems can be finely controlled by mesoscale geometry, enabling shock detonation at precise points [15, 16, 17]. 3-D-printable IPCs can also be used for shielding elements in satellites, where AM allows for greater geometric complexity and shock resistance in satellite housing components than traditional composite processing routes. However, despite these potential applications, the link between mesoscale geometry and mechanical properties is not well understood in complex IPC systems, and these applications are yet to be realized.

The aim of the present work is to investigate the relationship between mesoscale geometry and mechanical behavior of archtectured IPCs. First, we explore the quasi-static tensile energy absorption behavior of novel, 3-D printable IPCs, where we tailor geometric parameters to control failure behavior and maximize tensile energy absorption. We then examine the dynamic behavior of periodic architectured IPCs to relate the mesoscale unit cell geometry to the macroscale and fine-scale composite

shock response. These initial structure-property linkages are crucial in advancing the capabilities of this novel class of architectured IPCs.

This work is organized as follows. A brief review of relevant works is given in Chapter 2. The quasi-static tensile energy absorption study is described in Chapter 3. Chapter 4 presents the study on the dynamic behavior of architectured IPCs. Finally, the thesis is summarized in Chapter 5 with conclusions and future work.

Chapter 2

Background

2.1 Introduction

A better understanding of the energy absorption and shock behaviors of architectured interpenetrating phase composites (IPCs) is crucial for enabling their use in structural aerospace components. To gain insight into these behaviors of complex IPCs, we can first examine previous studies on traditional composites which describe geometry-induced damage and shock mechanisms that we can extend to our more complex composite systems. Furthermore, additive manufacturing (AM) has previously been used to form IPCs with fine control over mesoscale geometry. The preliminary examples of 3-D-printable IPCs and the resulting damage mechanisms serve in part as inspiration for the IPCs with more complex mesoscale geometries presented in the present work. In this chapter, we briefly review previous work on these topics: the energy absorption and shock behaviors of traditional composite structures, and the preliminary studies on AM IPCs which motivate this work.

2.2 Energy Absorption Behavior of Traditional Material Systems

Monolithic brittle materials often have low toughness and strain-to-failure in tension, rendering them unusable for structural applications where tensile loads are often unavoidable. However, they generally have a unique combination of high-temperature strength and low density that makes them attractive candidates for use in extreme aerospace environments. One way to take advantage of these exceptional properties while mitigating their poor toughness is to form them into composites, which use internal geometric features to induce desirable failure mechanisms. Fiber-reinforced ceramic-matrix composites (CMCs), for instance, use a combination of fiber and matrix to increase toughness and strain-to-failure in tension as compared to their monolithic constituents due to several characteristic damage mechanisms. One significant tensile damage mechanism is frictional dissipation along the fiber/matrix interface, where energy is expended as fibers debond and pull through the matrix. Another key damage mechanism is matrix cracking: within a localized plastic zone, energy is absorbed as small matrix cracks form and propagate, and fibers bridge these cracks to prevent catastrophic failure. Finally, fiber extension and breakage require significant energy input due to their high volume fraction of roughly 40% within the composite [18, 19]. The resulting additional energy expenditure modes and inelastic straining lead to roughly an order of magnitude increase in fracture toughness as compared to monolithic ceramic material [20, 21].

More complex brittle-matrix composites rely on similar stress-transfer and damage delocalization mechanisms to enhance their toughness in tension. For example, woven and braided fiber-reinforced brittle-matrix composites use fiber tows to bridge matrix cracks and distribute loads around stress-concentrating features [20, 22]. With continued matrix cracking, the fiber reinforcement displaces and locks up to resist further deformation, leading to compression of the matrix material which adds an additional mode of tensile energy absorption. This lock-up behavior causes localized hardening, which locally arrests damage and forces displacement to continue elsewhere in the

composite, delocalizing damage and enabling high energy absorption [23, 24, 25].

The hardening and damage delocalization behaviors of woven and braided brittle-matrix composites are exemplified by the chain composite, developed by Cox et al. [23, 24, 26, 27, 28]. Chain composites consist of parallel chains embedded in a brittle matrix. Under a tensile load, adjacent chain links, initially relaxed, slide towards one another as the chain is drawn tight, causing the chain crowns to compress trapped filler material. Once the inner radii of the chains come into contact and experience lockup, further tensile deformation and resulting filler compression initiate in another location of the chain composite. Finally, individual chain links and the entire composite fail after all chain links have experienced lockup. By converting far-field tensile loading into local compression of the brittle matrix, a chain composite extracts plastic work from constituents that are normally brittle in tension.

Additionally, cellular solids such as foams and lattices are of interest for energy-absorbing applications, where the combination of structural geometry and porosity distribution makes them amenable for use in composite materials. Foams are characterized by a random distribution of struts, and their mechanical properties including strain-to-failure, yield strength, and Young's modulus are primarily determined by their relative density, which is generally less than 0.3 [29]. By comparison, lattice structures are defined as a periodic arrangement of struts, and they are broadly characterized by their connectivity. The connectivity of a lattice is traditionally described using Maxwell's stability criterion, given as

$$M = b - 2j + 3 \tag{2.1}$$

in two dimensions, and

$$M = b - 3j + 6 \tag{2.2}$$

in three dimensions, where b is the number of struts and j is the number of joints in the unit cell of a lattice. If $M < 0$, then the given lattice structure will deform by bending at the joints and is thus referred to as a bend-dominated structure. Note that foams are classified as bend-dominated structures due to their relatively low

connectivity. By contrast, if $M \geq 0$, then the lattice structure will deform through extension of individual struts and is referred to as a stretch-dominated structure. The energy absorption behaviors of these two types of lattice structures vary greatly. For a given relative density, stretch-dominated structures generally have a greater yield strength; however, bend-dominated structures are more suitable for energy-absorbing applications due to the difference in post-yield behavior. After stretch-dominated structures yield in tension, their strength drops significantly, leading to minimal energy absorption during post-yield crush-up. Bend-dominated structures, by contrast, maintain a relatively constant crush-up stress, which is ideally equal to their yield stress, until reaching densification. Bend-dominated structures, including foams, are thus preferred as lightweight energy absorbers [30, 31]. The energy absorbing properties of foams and lattices, together with the damage behvaiors observed in traditional composites, are useful mechanisms in the design of architectured IPCs.

2.3 Shock Behavior of Composites and Preliminary Work

The shock response of traditional material systems including monolithic solids, laminated composites, and granular media has been studied extensively. Several models which stem from mass, momentum, and energy conservation laws accurately describe the shock behavior of monolithic solids, and macroscale shock properties such as the Hugoniot relation, shock front rise time, and strain rate-stress relation have been experimentally measured for an extensive list of materials [32, 33, 34, 35, 36]. While monolithic materials are treated as homogeneous in their shock response, the shock response of laminated composites is strongly influenced by interfacial effects. Interface scattering, the most prominent interfacial effect in laminated composites, induces geometric dispersion and spatial dissipation which cause the macroscale shock properties of laminated composites to deviate from those of their monolithic constituents. For instance, in laminated composites with layers of alternating metal and polymer,

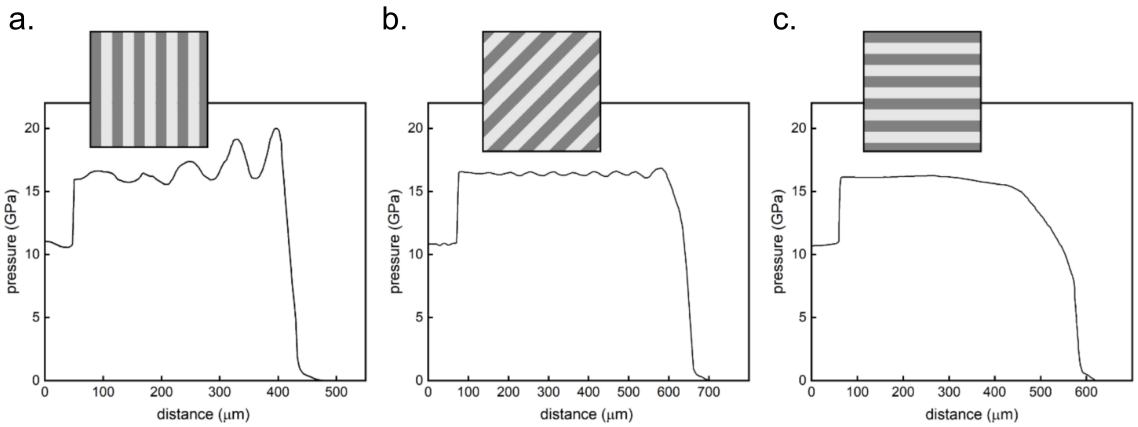

Figure 2-1: Pressure response of laminated composites with layers (a) perpendicular, (b) angled, and (c) parallel to the impact direction [38].

the shock velocity in the composite is below the range bounded by the Hugoniot of its constituents; the shock front rise time is greater than those of its monolithic constituents by more than an order of magnitude; and in the relationship between strain rate and stress represented by $\dot{\epsilon} \propto \sigma^n$, $n \approx 2$, where $n \approx 4$ for monolithic materials. Taken together, these differences in macroscopic shock properties indicate that internal interfaces slow and spread a shock front within laminated composites, increasing the shock viscosity of laminated composites relative to monolithic constituent materials [6, 37]. Furthermore, the laminate orientation has a strong effect on both macroscale shock properties and fine-scale shock response, as shown in Fig. 2-1, where internal wave reflections and interfacial redirection determine the oscillatory behavior of the pressure response in laminated composites. In particular for laminated composites of Al and Ni, intense heating and shearing occur at interfaces that are non-perpendicular to the shock direction, serving as an additional mode of shock dissipation [38, 39]. Altogether, the interfacial effects of 1-D laminated composites result in a shock response that is strongly dependent on material and geometric parameters including constituent impedance mismatch, interfacial density, laminate orientation, and interfacial bonding [6, 38].

Similarly, the shock response of granular media reflects their relative geometric complexity, where the random distribution of particles, voids, and intergranular contacts increases shock viscosity as represented by macroscale shock properties. For

instance, $n \approx 1$ in the strain rate-stress relationship of granular tungsten carbide due to interfacial effects such as shock front nonlinearities and multiple-wave interactions [40]. The random geometric arrangement also contributes to spreading of the shock front, where particles that begin in contact can transmit the shock wave faster than particles separated by voids. The resulting shock front width in granular WC is on the order of several particle diameters [41]. The geometric complexity also induces additional modes of macroscale energy dissipation, where upon compression, much of the longitudinal particle motion is converted to lateral momentum as particles shift to fill voids [40, 7]. Furthermore, the fine-scale shock response is dominated by geometry-dependent processes, where stress bridging and intergranular heating occur at randomly distributed intergranular contacts [42]. This strong dependence of shock response on particle distribution, considered together with the results of laminated composites, indicates that the internal geometry of more complex 3-D IPCs will have strong influence over their macroscale and fine-scale shock response.

One such IPC of current interest comprises a body-centered cubic (BCC) lattice of steel embedded within a matrix of aluminum. This material combination is attractive, first, for its viability in structural reactive systems, where the combination of steel and Al can provide the system with a desirable combination of strength and reactivity, respectively. Additionally, this IPC configuration can be reliably fabricated using AM processes. In particular, a print-then-infiltrate approach termed PrintCasting, depicted in Fig. 2-2, is commonly used for the steel-Al system. First, a steel lattice preform is 3-D printed. Next, Al is melted using an induction furnace. The lattice preform, with a greater melting temperature than the Al matrix, is then infiltrated with the motlen Al using a vacuum pump attached to the inlet nozzle. This two-step PrintCasting process provides a solution to the difficulties of printing A356/316L composites with fusion-based additive manufacturing processes, which otherwise cause aluminum and iron to form brittle intermetallic phases [13].

The behaviors of these PrintCast steel-Al IPCs have been thoroughly studied. For instance, in quasi-static tension, the interpenetrating nature of the structure gives rise to crack bridging and matrix cracking, leading to an order-of-magnitude increase in

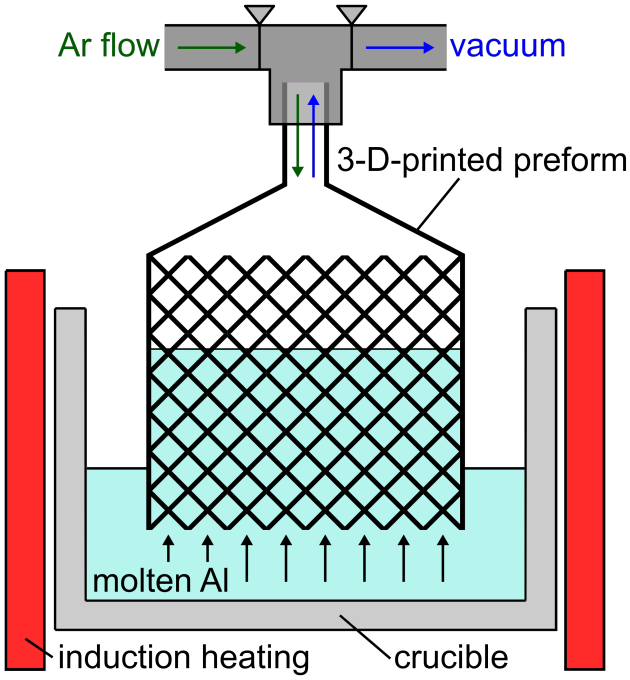

Figure 2-2: Schematic representation of the PrintCast process used to form metal interpenetrating phase composites.

tensile strain-to-failure as shown in Fig. 2-3 [13, 43, 44]. Functional properties, such as thermal conductivity, can also be linked to the internal mesoscale geometry and porosity of the structures [43]. Finally, ballistic impact tests demonstrate that in these IPCs, spallation, cratering, and delamination were limited by geometry-dependent scattering events [45]. These results together provide an initial demonstration of the strong linkage between mesoscale geometry and properties in novel, 3-D-printable IPCs.

To better understand the dynamic behavior of these steel-Al IPCs, a preliminary study examined plate impact simulations of a 2-D cross-section taken via micro-CT [46]. In the macroscopic shock response of the 2-D cross-section, the internal planar heterogeneities spread and slow the shock as shown in Fig. 2-4, and the resulting shock velocity lies below the range bounded by the Hugoniot of its constituents, similar to the effect seen in laminated composites. In the fine-scale, the shock front contours around the dense BCC steel lattice as it propagates into the composite, and angled interfaces induce transverse momentum through lateral wave dispersion. The

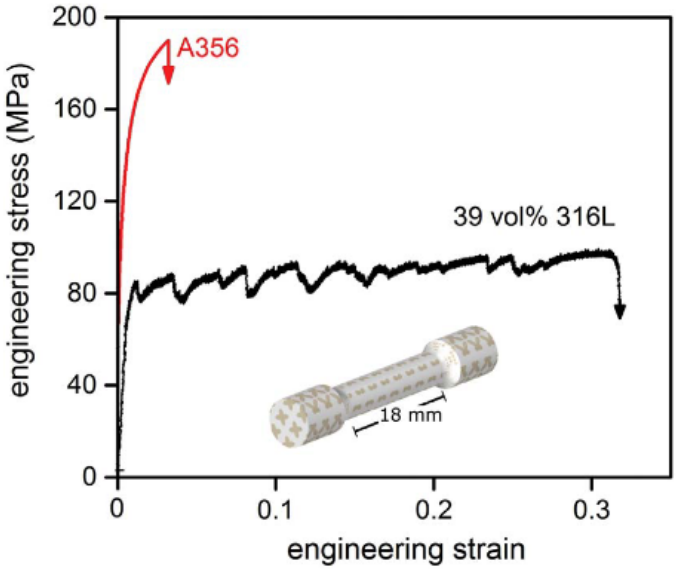

Figure 2-3: Tensile stress-strain curves for monolithic A356 Al and a BCC steel-Al IPC. From [13].

findings from these preliminary studies on architectured IPCs motivate the study the on dynamic behavior of 3-D IPCs in the work at present.

2.4 Summary

In summary, IPCs show promise for use in structural aerospace components due to their strong structure-property linkages. In traditional structural composite systems, such as fiber-reinforced, woven, and braided composites, interphase damage mechanisms mitigate flaw sensitivity and enhance energy-absorbing capability. Cellular solids also exhibit geometry-dependent failure mechanisms, where internal porosity causes desirable post-yield energy absorption behavior. With the fine control of mesoscale geometry granted by AM, we can thus induce and refine these damage mechanisms in IPCs to maximize energy absorption. And under high-rate loading, traditional laminated composites and granular media attenuate shock via interfacial effects, leading to geometric dispersion and spatial dissipation. Preliminary studies demonstrate qualitatively that IPCs exhibit similar shock behaviors due to internal geometry. However, the underlying geometry-dependent shock mechanisms are not

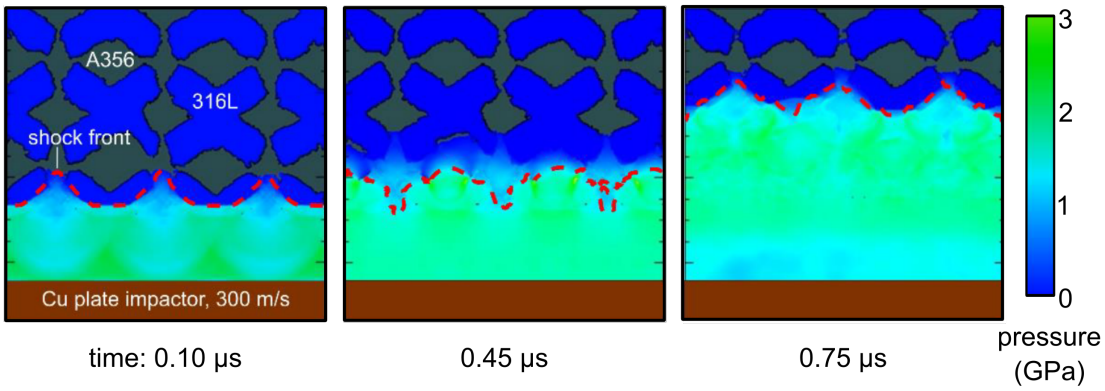

Figure 2-4: Shock front behavior in a 2-D cross-section of a BCC steel-Al IPC. From [46].

well understood, which hinders the capability of complex, 3-D-printable IPCs. In this thesis, we explore the linkages between mesoscale geometry and properties for IPCs—in particular, the energy absorption and dynamic behaviors—which are critical enablers for their use in structural aerospace components.

Chapter 3

Tensile Energy Absorption Behavior of Additively Manufactured Interpenetrating Porous Composites

3.1 Introduction

Given the desirable deformation mechanisms of traditional composites, we aim in this work to maximize the tensile energy absorption of interpenetrating phase composites (IPCs) with complex, tailorable mesoscale geometries. To this end, we leverage the net-shaping capabilities of additive manufacturing (AM) to tailor the energy absorption behavior of a 3-D-printable, architectured IPC called the chain lattice, depicted in Fig. 3-1. Inspired by the mechanics of traditional composites (described in Section 2.2), the chain lattice is a composite of two interpenetrating cellular solids: a chain reinforcement and a filler material. The chain reinforcement consists of links that displace towards one another under an applied tensile load. These links can lock-up and cause load transfer and damage delocalization, similar to the links in a chain composite. The filler, printed from the same material as the chain links, is a porous matrix that occupies the space between links and is compressed as the links displace, acting as a foam to densify and absorb energy under a far-field tensile

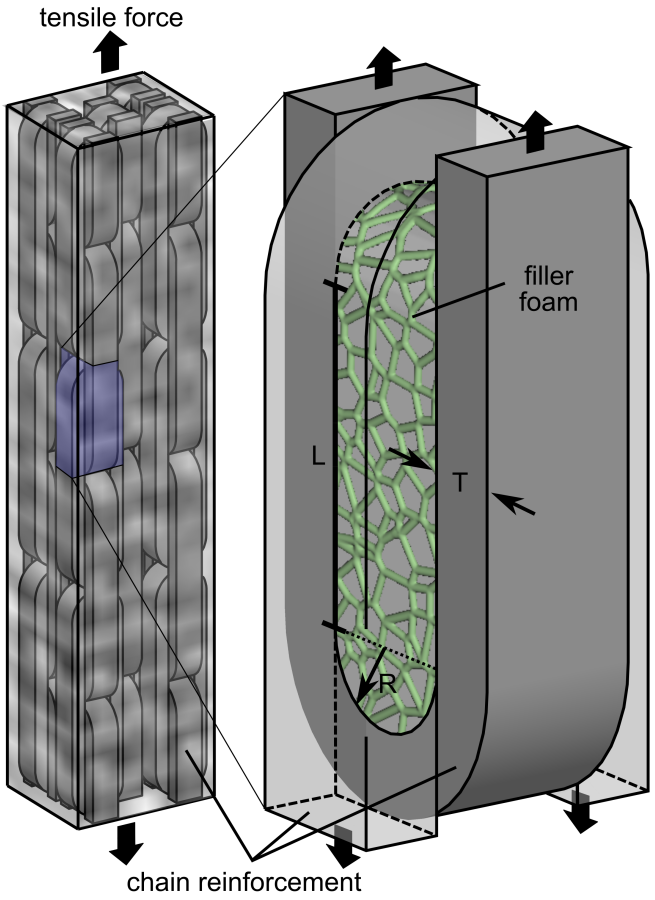

Figure 3-1: Chain lattice comprising a unidirectional chain reinforcement embedded in a random foam of the same base material. Key features of the racetrack chain links (thickness T, length L, crown radius R) are labeled in the magnified view of the half-unit cell.

load. This composite action—the displacement of the chain reinforcement together with the densification of the porous matrix—results in delocalized damage and high strain-to-failure in materials that are brittle when fully dense. Furthermore, both the chain reinforcement and the filler material are 3-D printed from the same material in a single print, allowing for net-shaping of chain lattices with fully tailorable strength and energy absorption. Note that this chapter is adapted from the published article [47].

3.2 Analytical Model for Energy Absorption

We first present guidelines for designing chain lattices that exhibit delocalized damage and high specific energy absorption in tension. The specific energy absorption of a chain lattice, W_s, is given by the general equation

$$W_s = \frac{\sigma\varepsilon}{\rho_o\tilde{\rho}}, \tag{3.1}$$

where σ is the tensile flow stress, ε is the strain-to-failure, ρ_o is the density of the fully dense parent material, and $\tilde{\rho}$ is the relative density of the chain lattice. Accordingly, optimizing W_s requires minimizing the overall density $\rho_o\tilde{\rho}$ and maximizing the volumetric work $\sigma\varepsilon$.

The relative density of a chain lattice is a volume-average of the densities of its constituents:

$$\tilde{\rho} = V_r + V_f\bar{\rho}, \tag{3.2}$$

where $\bar{\rho}$ is the relative density of the filler matrix, given by the ratio of the filler density to the density of the chain link material, and V_r and V_f are the volume fractions of the chain reinforcement and the filler, respectively. We note that while the filler and chain links can generally be formed from different materials, this work only considers chain lattices with filler and chain links of the same parent material, such that the entire chain lattice can be produced in a single print.

The tensile flow stress of a chain lattice σ is given by the product of the area fraction of the filler perpendicular to the loading axis, A_f, and the compressive flow stress of the filler, σ_f. We estimate σ_f using the standard power-law relation between the compressive strength of a cellular solid and its relative density ($\bar{\rho}$):

$$\sigma_f \approx C\sigma_o\bar{\rho}^n, \tag{3.3}$$

where C is a proportionality constant, σ_o is a material property, and the exponent n depends on nodal connectivity. For open-cell foams and bend-dominated lattices where strut connectivity is less than 12, $C \approx 0.3$, σ_o is the modulus of rupture of a

strut, and $n \approx 1.5$; for stretch-dominated lattices where strut connectivity is greater than 12, $C \approx \frac{1}{3}$, σ_o is the compressive strength of the fully dense material, and $n \approx 1$ [31, 29].

Using this flow stress model, we can tailor the strength of the filler to achieve delocalized damage, meaning that the filler undergoes crush-up and the chain links reach lockup before ultimate failure occurs. To develop this delocalized damage criterion for the chain lattice, we adapt a model developed by Gong et al. for the delocalized damage criterion of a chain composite [26], which requires that the maximum tensile stress in a chain link not exceed its tensile strength. The model considers stress contributions from four sources: the tensile stress along the outer surface of the chain crown; the compressive stress along the inner surface of the crown; shear tractions tangential to the interface of the two phases in the crown; and shear tractions tangential to the interface of the two phases along the leg. Applying this model to the chain link geometry shown in Fig. 3-1 gives

$$\sigma_r \geq \sigma_f \left[\frac{R}{T} C_1 + \frac{R+T}{T} C_2 + \left(1 + \frac{T}{2R}\right) C_3 + \frac{4L}{T} C_4 \right], \tag{3.4}$$

where σ_r is the tensile strength of the chain reinforcement, $C_1 = 2.57$, $C_2 = 1$, and $C_3 = C_4 = 0.5$ for fully bonded interfaces [26]. For chain lattices made from a brittle parent material, σ_r must account for size effects on tensile strength using Weibull statistics [48]. Since critical flaws of a given stress state are more likely to be present in specimens with a larger volume, the tensile strength of the reinforcement decreases with chain link volume according to the relationship

$$\sigma_r = \sigma_T \left(\frac{V_o}{V_1} \right)^{\frac{1}{m}}, \tag{3.5}$$

where σ_T is the tensile strength of a brittle material with representative volume V_o, V_1 is the volume of the specimen, and m is the Weibull modulus, which characterizes the volume effect on strength knockdown. Thus, the tensile strength of the chain reinforcement decreases as unit cell volume increases, and the compressive strength of

the filler foam must be tailored accordingly to satisfy the delocalized damage criterion. Inserting Eq. 3.3 and 3.5 into Eq. 3.4, the delocalized damage criterion for a chain lattice made from a brittle parent material follows as

$$\sigma_T \left(\frac{V_o}{V_1}\right)^{\frac{1}{m}} \sigma_o \bar{\rho}^n \left[\frac{R}{T}C_1 + \frac{R+T}{T}C_2 + \left(1+\frac{T}{2R}\right)C_3 + \frac{4L}{T}C_4\right], \tag{3.6}$$

where the left-hand side of the equation represents the tensile strength of the chain reinforcement with respect to a normalized volume, and the right-hand side represents the maximum tensile stress in the chain link due to compression of the filler.

The tensile strain-to-failure of a chain lattice can vary dramatically depending on the damage behavior. At one extreme, chain links fail before filler compression and chain lockup occur, resulting in localized damage and a strain-to-failure similar to that of the fully dense parent material. At the other extreme, delocalized damage can give rise to two distinct limiting behaviors based on the filler compression process. For chain lattices with the chain link geometry shown in Fig. 3-1, if the filler remains trapped between the chain links, then the strain-to-failure of the chain lattice is approximately

$$\varepsilon \approx \frac{(L+2R)(1-1.4\bar{\rho})}{L+2R+2T}, \tag{3.7}$$

where the term $(1-1.4\bar{\rho})$ is the predicted densification strain of the filler ε_D [29]. If instead the filler is ejected from the chain lattice during filler crush-up, then the maximum strain-to-failure is

$$\varepsilon \approx \frac{L+2R}{L+2R+2T}. \tag{3.8}$$

Using these models for σ, ε, and $\tilde{\rho}$, we predict specific energy absorption by substituting Eq. 3.2, 3.3, and 3.7 into Eq. 3.1 while assuming delocalized damage, completely trapped filler, and a constant flow stress, giving

$$W_s = A_f C \sigma_o \bar{\rho}^n \left(\frac{V_o}{V_1}\right)^{\frac{1}{m}} \frac{(L+2R)(1-1.4\tilde{\rho})}{L+2R+2T} \left[\rho_o(V_r + V_f\bar{\rho})\right]^{-1}. \tag{3.9}$$

3.3 Experimental Validation

3.3.1 Procedure

To validate this analysis, we performed tension tests on chain lattices fabricated on a Formlabs Form 3 stereolithography printer using the Formlabs poly(methyl methacrylate) Clear resin, which has a theoretical density of 1.19 g/cm^3. The chain lattices comprised chains embedded in a random, open-cell foam, as illustrated in 3-1. To assess the transition from localized to delocalized damage, we systematically varied the relative density of the filler foam while holding fixed the chain link geometry with $R = 9$ mm, $T = 5$ mm, and $L = 15$ mm. To adjust the relative density of the foam, we used a constant ligament diameter of 0.5 mm and varied the mean cell size from 2.3 mm to 4 mm. These values gave filler foam relative densities $\bar{\rho}$ between 0.13 and 0.28, corresponding to overall relative densities $\tilde{\rho}$ between 0.25 and 0.58 for the chain lattice. The foams were designed using random node generation in nTopology. The chain lattices had a gauge length of 12 cm and a square 9×9 cm^2 cross-section, with chains aligned parallel to the loading axis in a 3×3 array and each chain comprising approximately five links, as shown in Fig. 3-2. On average, between 8 and 12 cells of foam spanned the distance between the legs of the chain links.

For comparison, we performed tension tests on fully dense specimens that had a gauge length and diameter of 50 mm and 7 mm, respectively, and monolithic foam specimens with the same structure as the filler foam. The monolithic foam tensile specimens had a gauge length of 48 mm and a gauge diameter of 20 mm, with mean unit cell size ranging from 3 mm to 5 mm and a constant strut diameter of 0.625 mm. These values gave $\bar{\rho}$ ranging from 0.10 to 0.28 with 10 to 15 unit cells spanning the gauge diameter. Prior to testing, we cured all specimens in a UV oven for 30 minutes at 60°C, following the procedure recommended by Formlabs. We conducted the mechanical tests at room temperature using an electromechanical load frame with an initial strain rate of 10^{-3} s^{-1}. For the fully dense material and the foam specimens, we recorded strain using optical displacement measurements; for the chain lattices, we measured strain using the crosshead displacement.

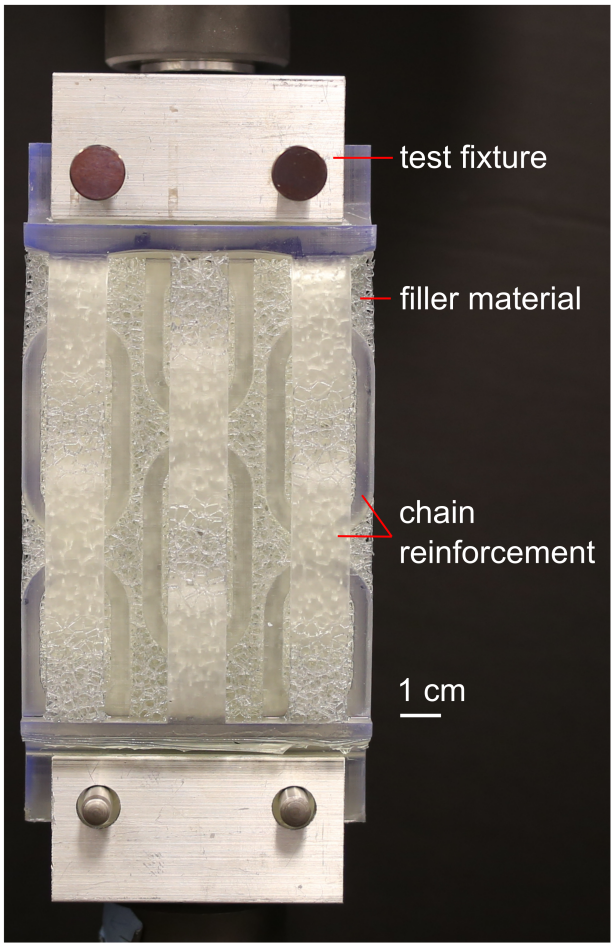

Figure 3-2: Exemplar chain lattice used for tension testing, where the individual chains are arranged in a 3×3 array embedded within the filler matrix.

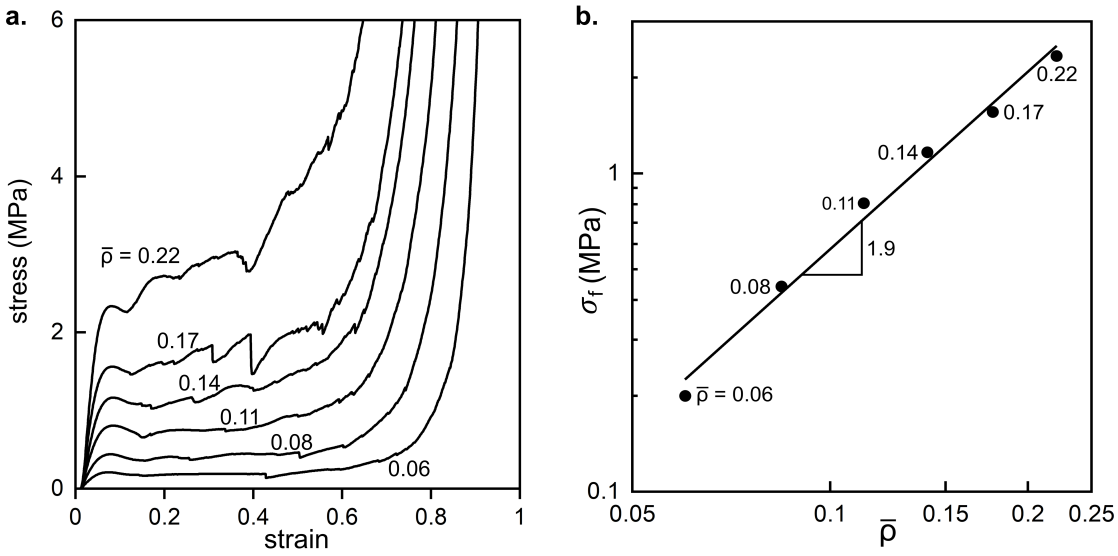

Figure 3-3: (a) Compressive stress-strain data and (b) compressive strength vs. relative density for 3-D-printed poly(methyl methacrylate) filler foams with varying relative densities.

Additionally, to calibrate Eq. 3.3 for poly(methyl methacrylate), we performed compression tests on foams with the same structure as the filler. The resulting stress-strain data shown in 3-3 exhibits behavior expected of foams in compression, with initial yield followed by relatively constant plateau stress until densification. The observed densification strains were slightly less than those predicted by $\varepsilon_D = 1 - 1.4\bar{\rho}$. The logarithmic fit shown in Fig. 3-3b gives $C = 0.6$ and $n = 1.9$, which roughly agree with the predicted values of $C \approx 0.3$ and $n \approx 1.5$ for open-cell foams and bend-dominated lattices [29].

3.3.2 Results and Discussion

The tension test results for the fully dense material and tensile foams are summarized in Fig. 3-4. The fully dense material failed at a peak stress of 70 MPa with a strain-to-failure of 4%. This relatively ductile behavior suggests that for this material, we can neglect strength knockdown due to volume effects and assume the limiting case for Eq. 3.5 in which $m \to \infty$. Foams with $\bar{\rho}$ ranging from 0.10 to 0.28 experienced strain-to-failure between 3% and 6%, which reflects their defect sensitivity and in-

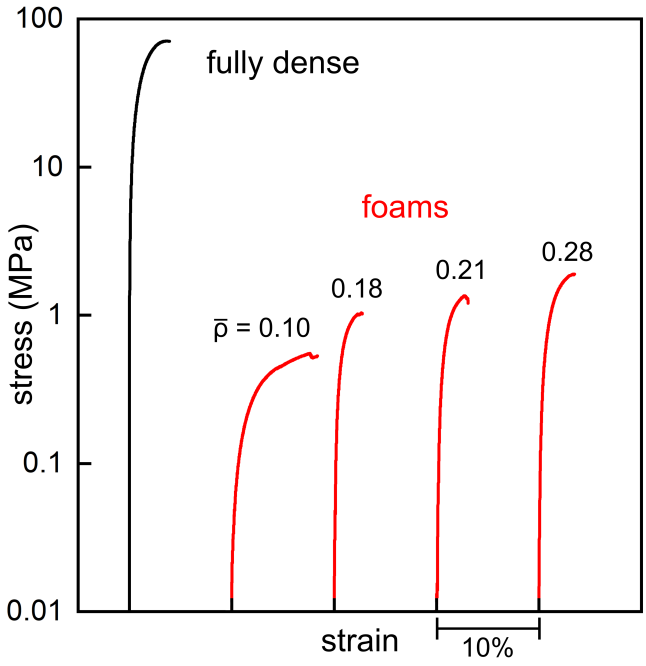

Figure 3-4: Tensile stress-strain data for 3-D-printed poly(methyl methacrylate) as a fully dense material and as filler foams with varying relative density $\bar{\rho}$.

trinsic brittleness in tension as compared to foams in compression [49]. Foam tensile strengths ranged from 0.5 to 1.9 MPa, slightly less than the compressive strengths of 0.5 and 3.7 MPa predicted using Eq. 3.3 with the calibrated values of $C = 0.6$ and $n = 1.9$.

Fig. 3-5 shows the stress-strain data of the chain lattices with $\bar{\rho}$ ranging from 0.13 to 0.28 (shown in parentheses), resulting in $\tilde{\rho}$ ranging from 0.25 to 0.58. The chain lattices with $\tilde{\rho} = 0.25$, $\tilde{\rho} = 0.31$, and $\tilde{\rho} = 0.37$ exhibit delocalized damage as they experienced filler foam crush-up before chain link failure. The delocalized damage process is best demonstrated by the chain lattice with $\tilde{\rho} = 0.25$, where in the stress-strain data of Fig. 3-5, the first peak of 0.6 MPa and the following stress drop correspond to tensile fracture of the filler foam in a plane between chain crowns. Next, the stress increases during compression of the filler foam as two planes of newly freed chain links slide towards one another to reach lockup, with crush-up stress of about 0.5 MPa. This process occurred a total of five times due to the five chain links in each chain and corresponding to the five peaks in the stress-strain data. Ultimate

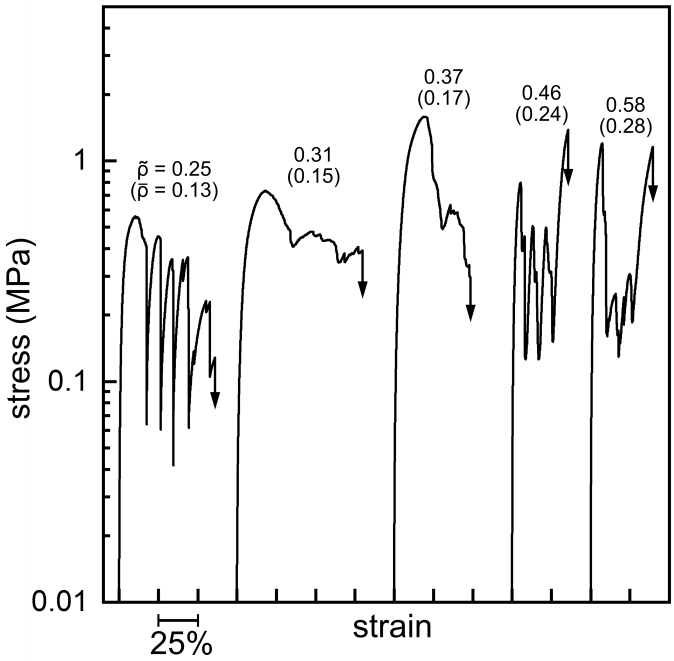

Figure 3-5: Tensile stress-strain data for 3-D-printed poly(methyl methacrylate) chain lattices with overall relative density $\tilde{\rho}$ ranging from 0.25 to 0.58 and filler relative density $\bar{\rho}$ (in parentheses) ranging from 0.13 to 0.28.

failure occurred only after all chain links experienced lockup, once individual chain links began to fail in the junction between the leg and the chain crown. The observed crush-up stress of 0.5 MPa agrees with the predicted crush-up stress of 0.5 MPa given by the product of the filler foam area fraction (0.576) and the compressive strength of the filler foam with $\bar{\rho} = 0.13$ (predicted as 0.87 MPa by Eq. 3.3). Furthermore, the observed strain-to-failure was 65%, which closely agrees with the 63% predicted by Eq. 3.7.

While the chain lattices with $\tilde{\rho} = 0.31$ and $\tilde{\rho} = 0.37$ also exhibited delocalized damage, they experienced comparatively constant plateau stresses rather than recurring stress peaks because multiple filler regions simultaneously underwent compression until the chain links reached lockup. For the chain lattice with $\tilde{\rho} = 0.31$, the observed strain-to-failure of 0.75 lies between the 0.61 predicted by Eq. 3.7 and the 0.77 predicted by Eq. 3.8 due to filler ejection during crush-up. For the chain lattice with $\tilde{\rho} = 0.37$, ultimate failure occurred before all chains reached lockup, resulting in incomplete crush-up and an observed strain-to-failure of 0.49, less than the predicted

0.58. And while the peak stress of 0.73 MPa for the chain lattice with $\tilde{\rho} = 0.31$ is roughly equal to the expected value of 0.66 MPa, the peak stress of 1.59 MPa for the chain lattice with $\tilde{\rho} = 0.37$ well exceeds the 0.83 MPa predicted by Eq. 3.3.

By comparison, the chain lattices with $\tilde{\rho} = 0.45$ and $\tilde{\rho} = 0.58$ experienced localized damage as several chains fractured before the filler began to crush-up. In both cases, the initial stress peaks in the stress-strain data of Fig. 3-5 represent failure of roughly half of the chain links and surrounding filler foam in the plane of failure. Next, several remaining chain links pulled through the weakened filler foam until reaching lockup. The chain lattices then failed once these chain links reached lockup, before filler crush-up could begin elsewhere in the specimen. This localized damage led to respective strains-to-failure of 0.36 and 0.40 which fall below the 0.51 and 0.47 predicted by Eq. 3.7. Furthermore, the inconsistent crush-up stresses which peak at roughly 0.50 MPa and 0.30 MPa fall far below the 1.6 MPa and 2.2 MPa predicted by Eq. 3.3, reflecting the minimal crush-up following initial localized damage and fracture.

These contrasting delocalized and localized damage mechanisms suggest that with geometric parameters $R = 9$ mm, $L = 15$ mm, and $T = 5$ mm, the transition from delocalized damage to localized damage occurs before $\bar{\rho} = 0.24$. Although this value is below the threshold of $\bar{\rho} = 0.33$ predicted by Eq. 3.6 for a bend-dominated foam, the observed transition agrees with the predicted $\bar{\rho} = 0.21$ under the assumption that the filler foam exhibits stretch-dominated behavior. The observation of stretch-dominated behavior at greater $\bar{\rho}$ is also supported by the elevated peak stress of the chain lattice with $\tilde{\rho} = 0.37$. Furthermore, the stress-strain data of the chain lattice with $\tilde{\rho} = 0.45$ displays characteristics of stretch-dominated behavior, with steep drops in stress after filler crush-up events.

We likely observe stretch-dominated behavior at elevated $\bar{\rho}$ values due to lateral constraint of filler foam by the chain legs, which gives rise to a multi-axial stress state in the filler. Lateral constraint of bend-dominated lattices during compression often results in stretch-dominated behavior [50]; this effect and the resulting increase in compressive strength are greater for foams with greater plastic Poisson's ratio $\nu_{plastic}$, which generally increases with $\bar{\rho}$ [51]. To observe this effect of $\bar{\rho}$ on $\nu_{plastic}$ for the

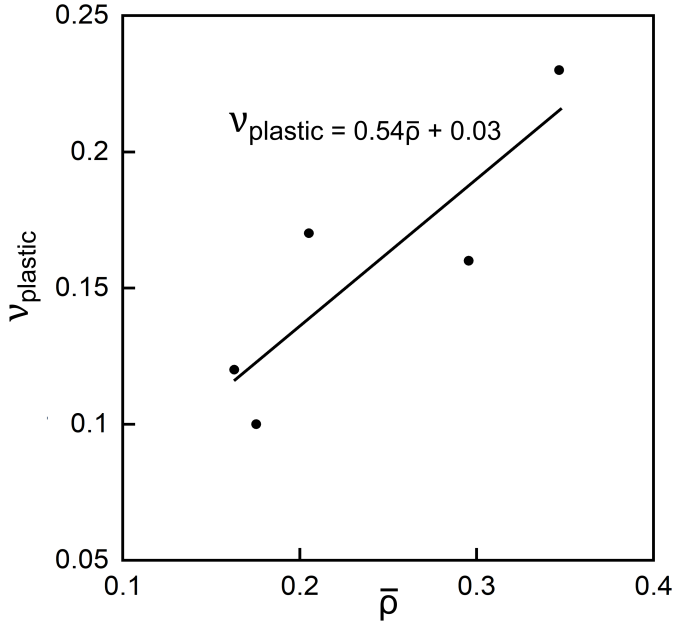

Figure 3-6: Plastic Poisson's ratio $\nu_{plastic}$ vs. relative density $\bar{\rho}$ for poly(methyl methacrylate) foams in compression.

chain lattice filler, we performed additional compression tests on foams with the same structure as the filler. We conducted the mechanical tests at room temperature using an electromechanical load frame with an initial loading rate of 100 N·min^{-1} up to a load of 500 N followed by a strain rate of 10^{-3} s^{-1}. Axial strain was measured using crosshead displacement, and radial strain was measured incrementally during testing with a micrometer. Fig. 3-6 shows the relationship between $\nu_{plastic}$ and $\bar{\rho}$. Notably, the linear fit predicts $\nu_{plastic} \approx 0$ for $\bar{\rho} = 0$ and $\nu_{plastic} \approx 0.5$ for $\bar{\rho} = 1$, which agrees with the theoretical $\nu_{plastic}$ of 0.5 for a fully dense incompressible material. This relationship supports the prediction of stretch-dominated behaviors at higher $\bar{\rho}$ due to lateral constraint, and we accordingly assume that the filler is limited by stretch-dominated behavior in the following calculations of the delocalized damage threshold.

The mechanical test results are summarized in Fig. 3-7, which shows specific energy absorption and tensile strength measurements for monolithic poly(methyl methacrylate), foams in tension and compression, and chain lattices with varying $\tilde{\rho}$

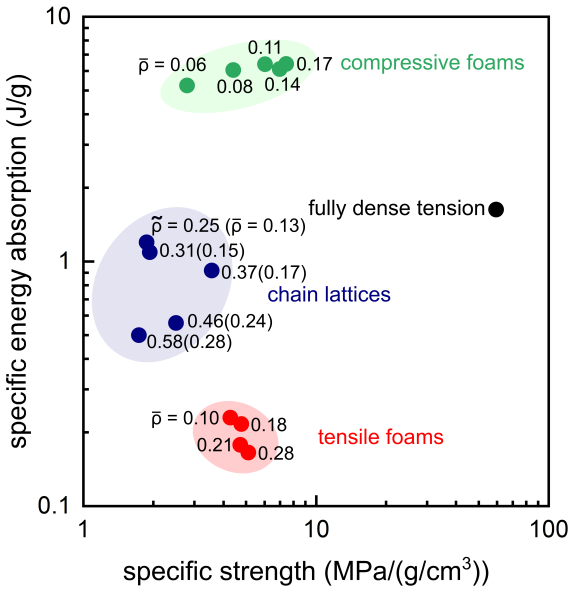

Figure 3-7: Specific energy absorption of chain lattices, compressive foams, tensile foams, and fully dense poly(methyl methacrylate). For the chain lattices, overall relative densities $\tilde{\rho}$ are followed by filler relative densities $\bar{\rho}$ in parentheses.

(with $\bar{\rho}$ in parentheses). While the flow stresses of the foams in tension were roughly in line with those of foams in compression, their low strain-to-failure led to specific energy absorption values between 0.16 and 0.23 J/g, more than an order of magnitude less than those of foams in compression with values between 5.2 and 6.4 J/g. By contrast, the delocalized damage process of the chain lattice resulted in a maximum observed specific energy absorption of 1.2 J/g for the chain lattice with $\tilde{\rho} = 0.25$. This observed value approaches the 1.6 J/g of the fully dense material and agrees closely with the 1.32 J/g predicted by Eq. 3.9. On the other hand, the chain lattice with $\tilde{\rho} = 0.58$, which experienced localized damage, had specific energy absorption of 0.5 J/g, far less than the 1.4 J/g predicted by Eq. 3.9 under the assumption of delocalized damage.

3.4 Parametric Analysis of Energy Absorption

Having experimentally validated our chain lattice model, we can use it to determine the effect of geometric parameters on specific energy absorption for chain lattices made from a brittle parent material. Here we assume ideally brittle, linear-elastic behavior, such that the specific energy absorption of the fully dense material is

$$W_{s,monolithic} = \frac{\sigma_T \varepsilon}{2\rho_o}, \tag{3.10}$$

with $\varepsilon \approx 0.1\%$. In our analysis, we evaluate a normalized specific energy absorption Ψ, defined as the ratio of chain lattice specific energy absorption (Eq. 3.9) to the specific energy absorption of the fully dense material (Eq. 3.10). We also limit the analysis to values of $\frac{R}{T}$ and $\frac{L}{T}$ such that

$$(1.4\bar{\rho})(2L + 2R) \geq R, \tag{3.11}$$

where the left-hand side of the inequality approximates the length of the compressed filler matrix and the right-hand side represents the inner radius of chain link crowns in contact. This excludes from the analysis cases in which the inner radii of the chain crowns come into contact before full compression, which would cause premature chain link failure in the crown-leg junction.

With these considerations, we first examine Ψ with varying $\bar{\rho}$ for chain lattices with fixed $\frac{R}{T}$ and $\frac{L}{T}$, similar to our experimental procedure. This relationship for chain lattices with both bend- and stretch-dominated filler is shown in Fig. 3-8. We set $m = 10$, which is the Weibull modulus of 3-D-printable SiOC and is typical of conventionally processed ceramics [52], and assume that the delocalized damage transition is limited by the strength of a stretch-dominated filler matrix, in line with our experiments. From Fig. 3-8, we observe that Ψ increases monotonically up to the delocalized damage threshold predicted by Eq. 3.6. This trend contrasts the observed relationship between specific energy absorption and $\bar{\rho}$ shown in Fig. 3-7 because Eq. 3.9 assumes that the crush-up stress is constant and equal to the compressive strength

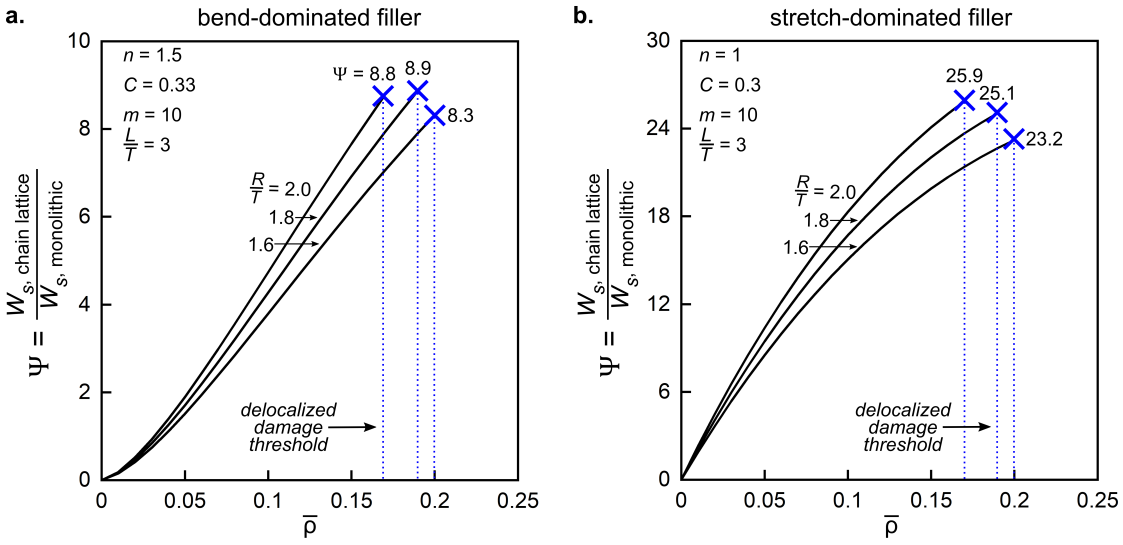

Figure 3-8: Normalized specific energy absorption Φ vs. relative density $\bar{\rho}$ for chain lattices with (a) bend-dominated and (b) stretch-dominated filler matrices, with $\frac{L}{T} = 3$, $m = 10$, and selected values of $\frac{R}{T}$.

of the filler. Instead, as shown in Fig. 3-5, we observe experimentally that the chain lattice crush-up stresses fluctuated below the initial filler foam yield stresses, resulting in non-ideal specific energy absorption.

We observe from Fig. 3-8 that for given values of $\frac{R}{T}$ and $\frac{L}{T}$, Ψ is maximized at the delocalized damage threshold. The threshold relative density values for variable $\frac{R}{T}$ and $\frac{L}{T}$ are shown in Fig. 3-9.

Using the delocalized damage threshold values shown in Fig. 3-9, we can then calculate maximum Ψ values with variable $\frac{R}{T}$ and $\frac{L}{T}$ using Eq. 3.9. These calculations are shown in Fig. 3-10, where, for a 3-D-printable ceramic like SiOC with $m = 10$ [52], and including the limitation given by Eq. 3.11, the maximum values of Ψ are 13.3 with $\frac{R}{T} = 1.9$, $\frac{L}{T} = 0.4$, and $\bar{\rho} = 0.29$ for chain lattices with bend-dominated filler, and 29.6 with $\frac{R}{T} = 2.2$, $\frac{L}{T} = 1.6$, and $\bar{\rho} = 0.20$ for chain lattices with stretch-dominated filler. This analysis suggests that forming SiOC into a chain lattice with stretch-dominated filler can improve tensile specific energy absorption from 0.2 J/g for the fully dense material to 5.9 J/g as a chain lattice. Interestingly, this order of magnitude increase in tensile specific energy absorption is similar to the increment in

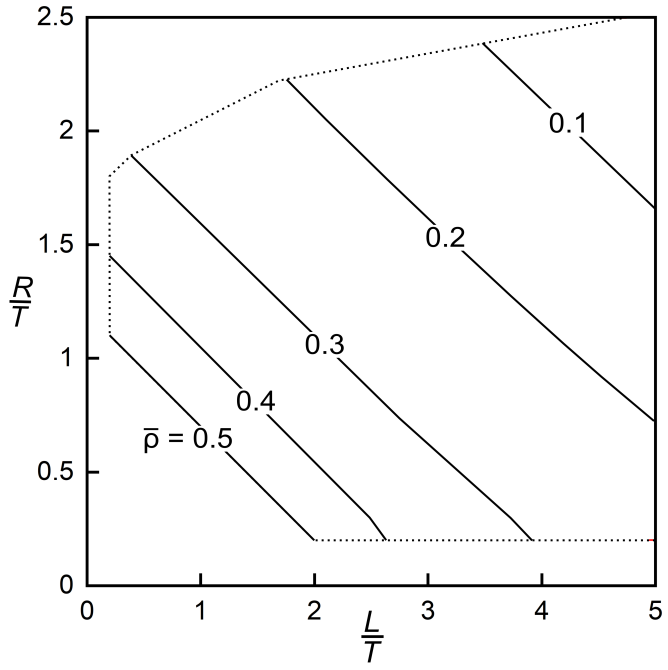

Figure 3-9: Contours of delocalized damage threshold $\bar{\rho}$ with variation in geometric parameters $\frac{R}{T}$ and $\frac{L}{T}$.

specific energy absorption when fully dense ceramics are formed into fiber-reinforced ceramic matrix composites [53].

3.5 Summary

With AM, we can finely control mesoscale geometry to tailor the quasi-static mechanical behavior of IPCs. In this chapter, we introduce the chain lattice, a 3-D-printable IPC comprising a chain reinforcement and a filler material, which uses the combined action of both phases to delocalize damage and inhibit catastrophic failure. First, we develop a model which uses material properties and geometric parameters to predict chain lattice tensile strain-to-failure and energy absorption. This model considers the criterion for delocalized damage, which places an upper limit on the relative density of the filler material with which the chain lattice will still experience delocalized damage.

We use this model as a guide to print and tensile test chain lattices printed from

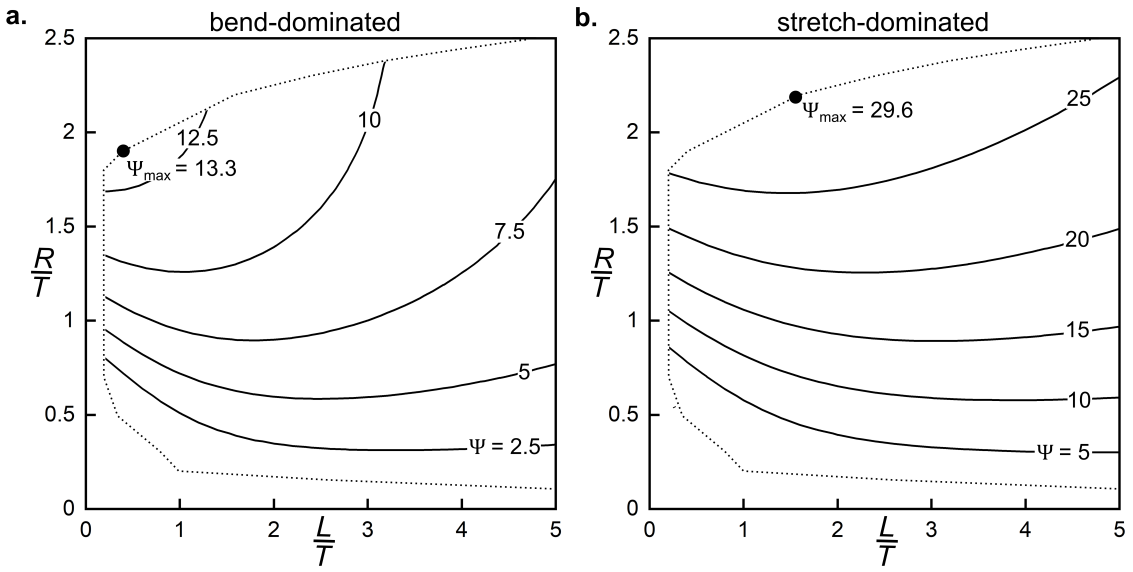

Figure 3-10: Normalized specific energy absorption Ψ for chain lattices with (a) bend-dominated and (b) stretch-dominated filler matrices.

poly(methyl methacrylate) with fixed chain link geometric parameters and varying filler material relative density. From these tests, we see that the delocalized damage criterion developed for the analytical model accurately predicts the filler material relative density at which the chain lattice no longer experiences delocalized damage. For the chain lattice that exhibited the most ideal failure behavior, our model closely predicts the strain-to-failure and specific energy absorption. These results serve to validate the analytical model, which we can then extend to ideal material systems and geometries.

Applying the model to an ideally brittle material, where we expect the greatest improvement in tensile specific energy absorption as compared to a monolithic parent material, we find that when optimizing chain reinforcement geometric parameters, our model predicts an increase in tensile specific energy absorption of more than an order of magnitude. This improvement is roughly equal to that seen when forming a ceramic into a CMC, indicating that this method of forming AM IPCs is a powerful tool for designing damage-tolerant structural components out of nominally brittle parent materials.

Chapter 4

Shock Response of Additively Manufactured Interpenetrating Phase Composites

4.1 Introduction

Previous studies demonstrate qualitatively that interpenetrating phase composites (IPCs) utilize geometry-dependent shock attenuation mechanisms such as interface scattering and geometric dispersion to enhance their shock viscosity relative to monolithic constituents [45, 46]. Considering these preliminary observations, the goal of the current work is to assess more rigorously both the macroscale and fine-scale shock response of architectured 3-D IPCs, which can enable a tailorable IPC shock response and make them useful for structural aerospace components. To this end, we performed 3-D plate impact simulations on the IPCs with the body-centered cubic (BCC) configuration previously discussed in Section 2.3, and we varied simulation parameters such as lattice volume fraction, impact orientation, and impact velocity to observe the geometry sensitivity of the shock response.

4.2 Plate Impact Simulation Setup

We peformed 3-D hydrocode simulations using CTH (version 12.2, Sandia National Laboratories, 2020). The simulation setup is shown in Fig. 4-1a. The simulated IPC comprised a BCC lattice of 316L stainless steel embedded within a matrix of A356 aluminum. The structure of the IPC was generated using an STL file of an idealized BCC microstructure such that there was no interfacial porosity. The BCC unit cell length was 2.5 mm and the diameter of the cylindrical struts was 0.8 mm, resulting in a steel volume fraction of 40%. We assumed no bonding between the constituents, which is observed in these IPCs experimentally [44]. The simulated composite contained three unit cells in the shock direction with an infinite A356 Al backer at the rear face to suppress spall. Boundaries in the lateral directions were modeled using periodic boundary conditions, while the boundaries in the shock direction were modeled as sound speed–based absorbing to allow material and stress to flow in and out of the simulation. Tracer points were arranged in a 3-D grid with spacing of 0.1 mm within the composite to record data every 5 ns. The equations of state for the steel, Al, and copper flyer were Mie-Gruneisen 316L steel, SESAME Al6061, and SESAME Cu, respectively. The constitutive strength models for the steel, Al, and Cu were Johnson-Cook 316L steel, Johnson-Cook Al6061, and Zerilli-Armstrong Cu, respectively. Fracture and contact were incorporated using CTH's internal boundary-layer algorithm.

In this work, our default simulation setup included a lattice volume fraction of 40%, impact orientation of [100], and impact velocity of 1000 m/s. To probe a range of particle velocities, we varied impact velocity from 500 m/s to 1500 m/s at intervals of 250 m/s. We also examined the effects of mesoscale geometry on shock response by varying geometric parameters as shown in Fig. 4-1b: we varied lattice volume fraction from 20% to 80% at intervals of 20% by increasing strut diameter, and along with the [100] orientation, we simulated impact along the [110] and [111] directions.

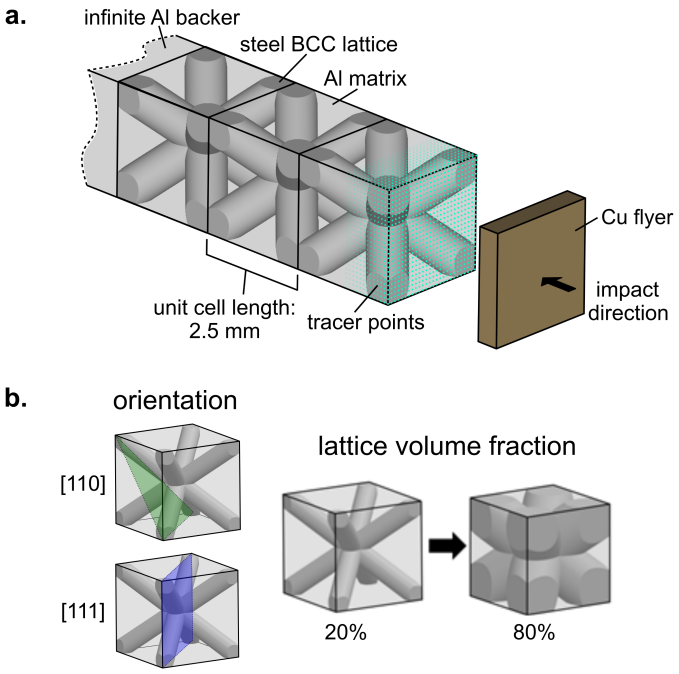

Figure 4-1: (a) Simulation setup and (b) variations in impact orientation and lattice volume fraction.

4.3 Macroscale Composite Shock Properties

The simulated composite shock velocity-particle velocity Hugoniot relation for lattice volume fraction of 40% is shown in Fig. 4-2a. Notably, the composite shock velocity lies slightly below the shock velocity predicted by kinetic energy averaging, a method often used to predict composite Hugoniot relations due to its relative simplicity and accuracy [54, 55], as given by

$$u_{mix}^2 = X_a u_a^2 + (1 - X_a) u_b^2. \tag{4.1}$$

In particular, the composite shock velocity is an average of 2.25% less than the kinetic energy average prediction. This reduction in composite shock velocity relative to its predicted value is similar to the shock velocity knockdown observed in laminated composites and in simulations of 2-D cross-sections of these IPCs [6, 46], similarly indicating that geometrically induced interface scattering increases shock viscosity in these composites. We note that by comparison, the reduction in shock velocity of

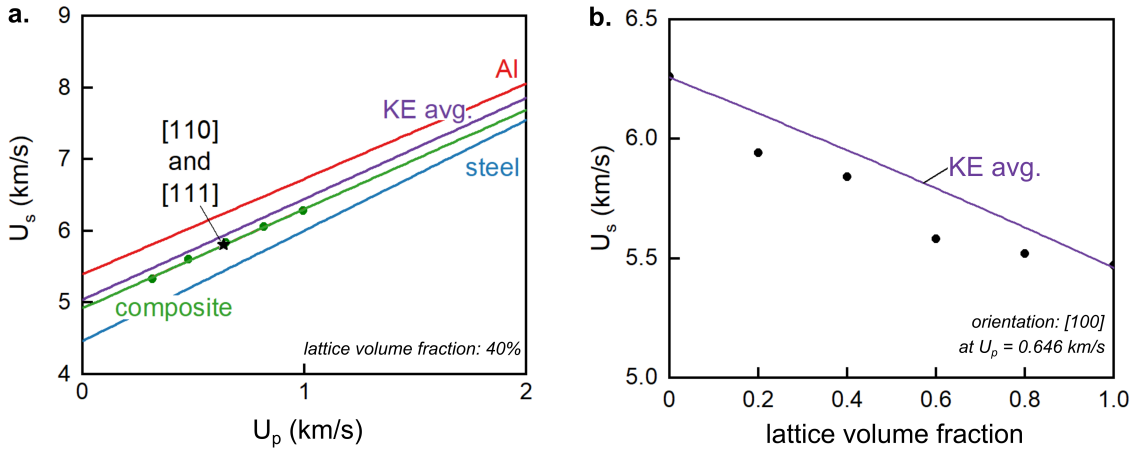

Figure 4-2: (a) Simulated composite Hugoniot relation compared to experimental Hugoniot relations of the constituent materials and a kinetic energy average prediction, with points from the simulated [110] and [111] impact orientations overlaid, and (b) simulated composite shock speed with varying lattice volume fraction.

laminated composites and 2-D cross-sections relative to their monolithic constituents are much greater than the reductions seen in the composites at hand; while the composite Hugoniots of laminated composites and 2-D cross-sections lie below the bounds predicted by the experimentally measured Hugoniots of their constituent materials, the composite shock velocities for these 3-D IPCs lie within the bounds of the constituents [35, 56]. This difference in relative shock velocity reduction is likely due in part to material effects. The laminated composites previously discussed were formed from alternating layers of metal and polymer [6], where the mechanisms governing shock transfer in polymers are influenced by microscale polymer packing and entanglement, generally resulting in slower shock transfer processes and leading to a slower shock velocity [57, 58].

The difference in relative shock velocity reduction is also likely due to differences in the openness of the structures, represented schematically in Fig. 4-3. In the architectured 3-D IPCs (cf. Fig. 4-3c), open channels within the 3-D structure allow much of the shock front to travel without encountering interfaces. By contrast, the laminated composites have no open channels, and the thin open channels within the 2-D cross-sections were an unintentional product of the location of the cross-section

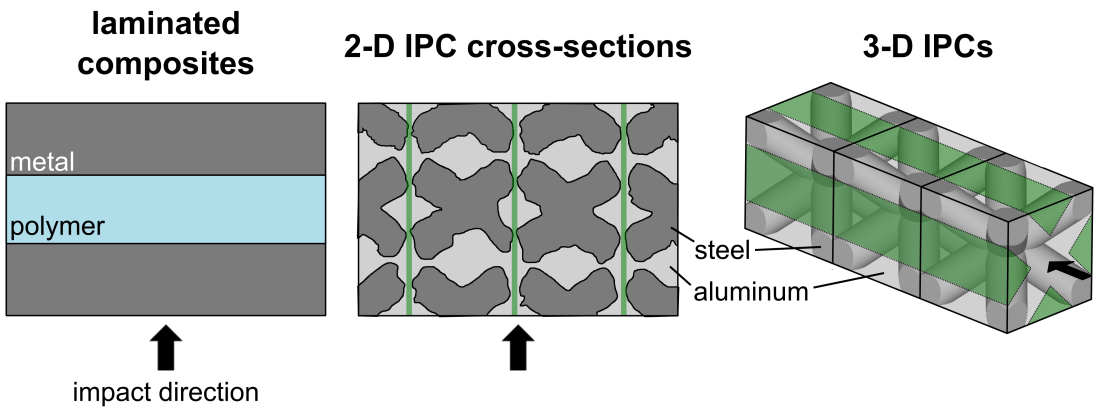

Figure 4-3: Schematic comparison of the structural openness within laminated composites [6], 2-D cross-sections of BCC IPCs [46], and 3-D IPCs, where open channels are represented in green.

plane and are exacerbated by inconsistency in manufacturing. These relatively closed structures within the laminated composites and 2-D cross-sections cause the entirety of the shock front to be slowed as it travels into the composites and encounters interfaces. Nevertheless, despite the relative openness of the 3-D IPC structure, the macroscale shock velocity measurements of the 3-D IPCs indicate that overall, the internal mesoscale geometry slows the shock front, thereby enhancing the macroscale composite shock viscosity.

In Fig. 4-2a, the shock velocities of the [110] and [111] orientations at impact velocity of 1000 m/s are overlaid as points. Notably, they coincide with the shock velocity of the original [100] configuration, suggesting that this macroscale quantity of shock velocity is insensitive to impact orientation and, more broadly, is likely insensitive to fine-scale lattice geometry. We also observe a slight knockdown in shock velocity when varying lattice volume fraction at a fixed particle velocity, as shown in Fig. 4-2b. Comparable to the knockdown of 2.25% in Fig. 4-2a, the composite shock velocity lies at an average of 2.5% below the kinetic energy average in Fig. 4-2b. This relatively constant, predictable knockdown in shock velocity further indicates that the macroscale shock velocity is relatively insensitive to fine-scale lattice geometry and is likely more strongly influenced by macroscale composite properties such as lattice volume fraction and connectivity of the structure.

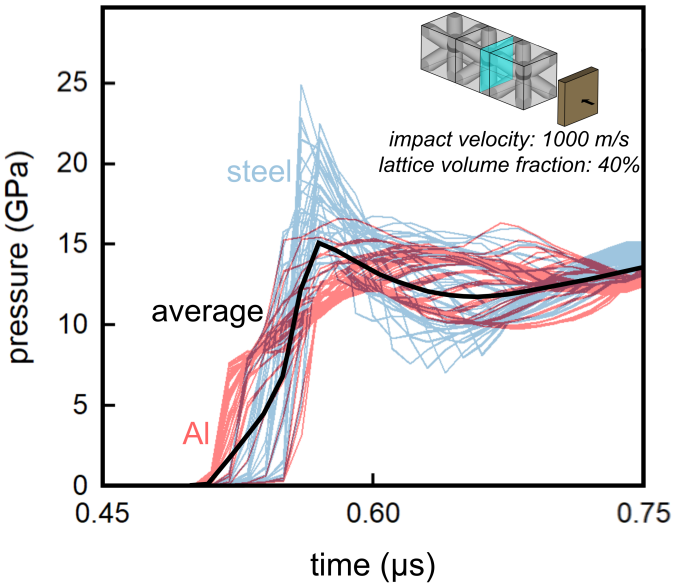

Figure 4-4: Pressure histories for tracer points and the plane average within a plane 3.2 mm into the composite with impact orientation of [100], impact velocity of 1000 m/s, and lattice volume fraction of 40%.

The ability of the composite to slow and spread shock is further demonstrated in Fig. 4-4, which displays the pressure history for tracer points located at a plane within the second unit cell from the strike face, allowing sufficient distance for interface interaction. Notably, we observe distinctly different pressure histories when measuring from tracer points within the steel lattice and from tracer points within the Al matrix. Looking first at the shock front measured from tracer points within the steel lattice, we observe a distribution of shock front arrival times that centers around the plane average, indicating that the shock front, ideally beginning as a planar discontinuity, has spread within the steel lattice. This spreading is likely due to lattice interactions which convert a fraction of the longitudinal motion of the shock front into transverse motion, where, upon contacting the angled struts of the lattice, the shock is redirected at an angle into the lattice by the 45-degree-angled interface. The resulting fraction of the shock front within the struts of the steel lattice is no longer parallel to the plane of the strike face, causing the distribution in shock front arrival times which is centered around the plane average.

In the pressure histories measured from the Al tracer points, we observe two distinct behaviors, where, depending on the tracer point, the shock front appears to arrive either before or after the plane average. This difference in behavior is due to the openness of the structure, as previously described and shown in Fig. 4-3. Within open channels of Al in the composite, the shock front can reach these tracer points without encountering any interfaces and thus travels with minimal impedance. On the other hand, at Al tracer points that lie between nodes of the BCC lattice (i.e., outside of the green regions of Fig. 4-3), the shock front is delayed due to lattice interactions, where shock transfer at heterophase interfaces induces a finite time delay, driving wave scattering. Altogether, these dispersive behaviors spread the shock front and increase its width, indicating that lattice-dependent geometric dispersion is a key mechanism of shock viscosity in these 3-D IPCs.

The shock front resulting from these behaviors is illustrated in Fig. 4-5, where the contour of the shock front is displayed at several time intervals after impact. Upon impact, the shock front initially propagates into the composite as a planar wave, as shown in the first screenshot at 5 ns. However, interfacial shock transfer slows the shock front as it encounters the dense steel lattice, and variation in the openness of the lattice structure causes the relative spread of the shock front as discussed previously. This combination of effects is clear even by 180 ns, where the contour of the shock front is dominated by the mesoscale geometry of the lattice. The two distinct behaviors within the Al matrix, discussed previously, are especially clear at 400 ns. In between steel nodes, the shock front is slowed due to lattice interactions. By contrast, the shock front faces minimal impedance in the open channels of the Al matrix (cf. Fig. 4-3). These contrasting shock histories, most visible at 400 ns, lead to the distinct behaviors in the pressure history of the tracer points within the Al as shown in Fig. 4-4.

As described earlier, the diagonal lattice-matrix interfaces redirect the shock front at an angle, converting some of the fully longitudinal shock front motion into transverse motion. This effect is shown more clearly in Fig. 4-6, where the ratio of transverse to longitudinal velocity is roughly ± 1 within the struts of the lattice, suggesting

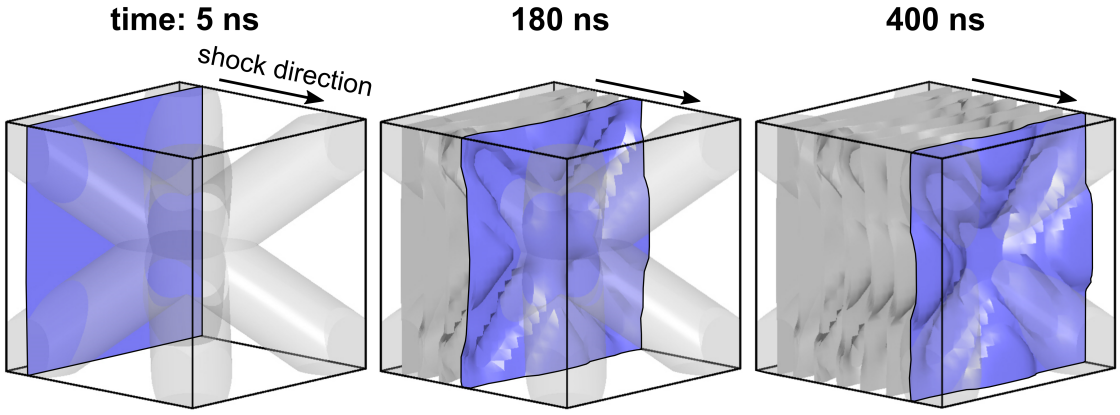

Figure 4-5: Contour of the shock front in the first unit cell from the strike face after 5 ns, 180 ns, and 400 ns.

that the shock front is moving at a 45-degree angle to the longitudinal direction due to the angling of the struts. By comparison, the maximum relative transverse velocity in granular media is roughly only 0.1 and is due solely to random particle and porosity distribution [40]. This large difference in the ratio $\frac{V_T}{V_L}$ when comparing 3-D IPCs and granular media indicates that compared to stochastic particles, the customized, periodic mesoscale geometry of the 3-D IPCs more strongly drives shock dispersion. Furthermore, the average transverse velocity taken over the entire volume of the composite approaches zero, reflecting the geometric symmetry of the lattice and indicating that this process is strongly dissipative. These connections between mesoscale geometry and shock behavior indicate that geometry controls both fine-scale dispersive and dissipative mechanisms.

Taken together, these geometric effects result in an average shock front rise time of roughly 200 ns, which is about an order of magnitude greater than the shock front rise time of roughly 20 ns observed in monolithic materials. This comparison further suggests that the mesoscale geometry of the 3-D IPCs enhances their relative shock viscosity [6, 39]. Using this shock front rise time, we can estimate shock front width Δ by

$$\Delta = (U_s - U_p)t_s, \tag{4.2}$$

where t_s is shock front rise time, U_s is composite shock velocity, and U_p is particle

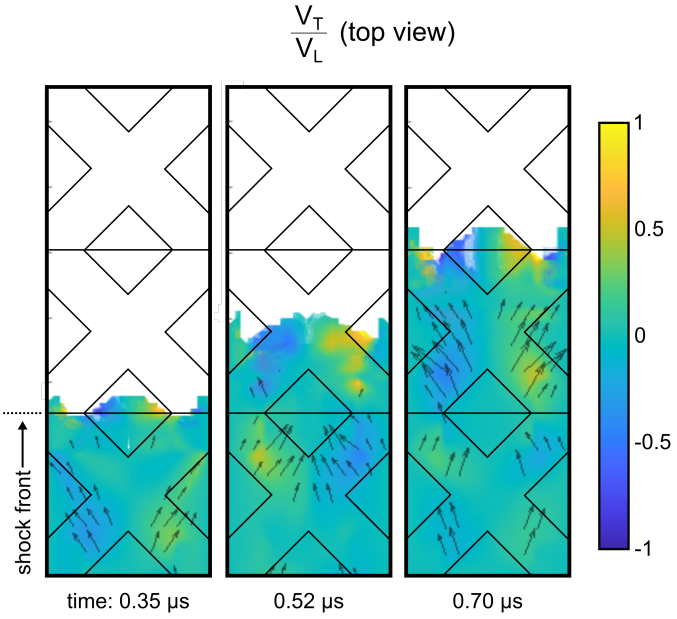

Figure 4-6: Transverse velocity, V_T, normalized by longitudinal velocity, V_L, at given times, with vectors overlaid to indicate shock velocity (top view). Shock parameters are the following: impact direction of [100], impact velocity of 1000 m/s, and lattice volume fraction of 40%.

velocity [42]. Using the aforementioned shock front rise time, with values of U_s and a composite-averaged U_p taken from Fig. 4-2, Eq. 4.2 gives an estimated shock front width in the composite of 1.04 mm. This relative length-scale for shock front width, on the order of the composite unit cell length of 2.5 mm, is similar to that seen in granular media and monolithic materials, where the shock front width is on the order of several particle diameters and several atomic spacings, respectively [36, 40]. We note that with more unit cells in the shock direction, the length-scale of the shock front width would likely increase to reach several unit cells, analogously matching that of monolithic solids and granular media.

Finally, we observe that within a propagation length-scale of several unit cells, the periodicity of the structure supports a steady wave. This ability to support a steady wave is demonstrated in Fig. 4-7, where, at planes of tracer points within different unit cells but at the same relative unit cell location, the pressure profiles are identical. This observation is more clearly shown in Fig. 4-8, where the plane average pressure

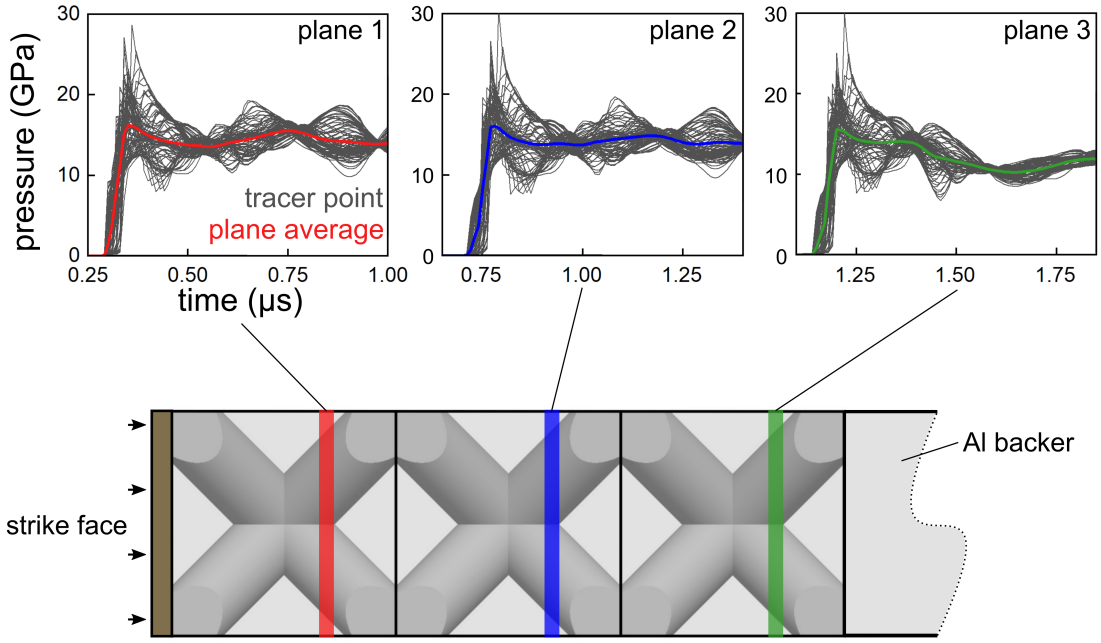

Figure 4-7: Pressure histories of 3 planes of tracer points taken from the same location within different unit cells.

profiles are overlaid. Note that in the rearmost plane of tracer points, there is a drop in stress that occurs due to the reflection of the release wave off of the Al backer which arrives at the rearmost plane. Notably, this steady wave behavior contrasts the behavior of laminated composites with layers oriented parallel to the shock direction, where distinctly different shock speeds within the constituent materials cause the shock front to spread indefinitely, resulting in an unsteady wave front [38].

Taken together, these geometry-dependent macroscale shock qualities—reduction in shock Hugoniot, increased shock front rise time and shock front width, and conversion of longitudinal motion into transverse motion—indicate that the internal mesoscale geometry of these 3-D IPCs leads to slowing and spreading of the shock wave, enhancing composite shock viscosity relative to its monolithic constituents. In the following section, we further explore the relationship between internal mesoscale geometry and shock response by examining several elements of the fine-scale shock response.

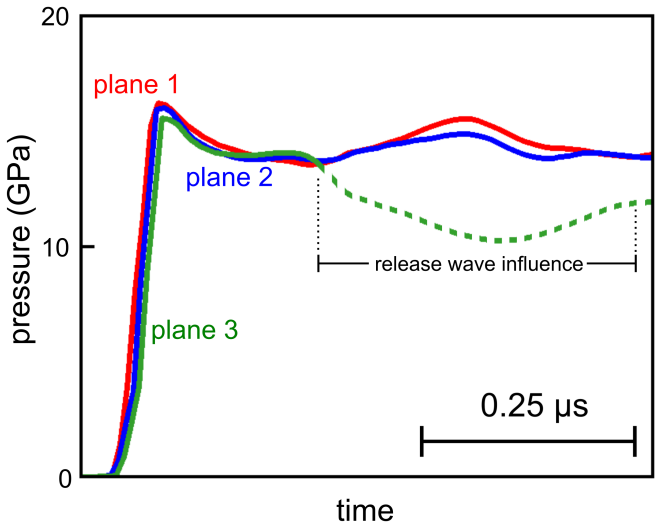

Figure 4-8: Plane-average pressure histories from the planes in Fig. 4-7 overlaid.

4.4 Fine-Scale Shock Response

4.4.1 Oscillatory Behavior

In the fine-scale, several aspects of the composite shock response are oscillatory in nature. The oscillatory behavior of the pressure response, for instance, is shown in Fig. 4-9a, where the pressure history is measured from the tracer point in the center of the BCC unit cell as denoted in Fig. 4-9b.

To better understand this oscillatory pressure response, we can link several aspects of the oscillations to both composite geometry and material properties. To this end, we first examine the initial peak pressure of 19.11 GPa from Fig. 4-9a. We can predict the initial peak pressure by using the pressure-particle velocity Hugoniot relation [36], given as

$$P = \rho(C_0 + SU_p)U_p, \tag{4.3}$$

where P is pressure, ρ is material density, C_0 is the material sound velocity at zero pressure, S is an empirical shock parameter, and U_p is particle velocity. From Eq. 4.3, we see that in order to calculate P, we first have to find U_p within the steel, where the material properties ρ, C_0, and S can be readily found in material databases [35].

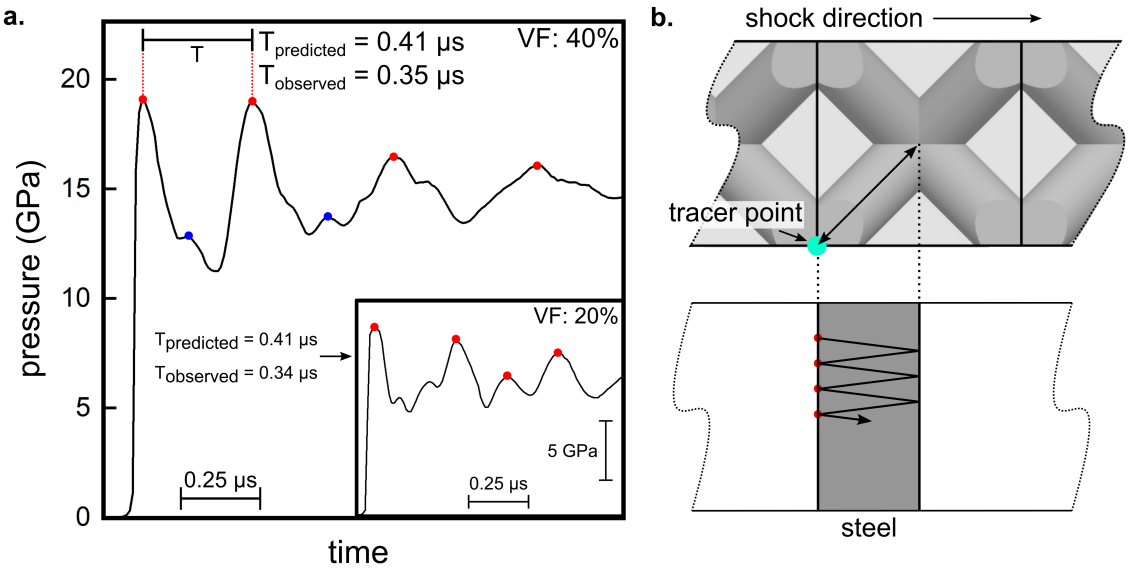

Figure 4-9: a) Pressure history for the tracer point located at the central node of the BCC unit cell for a lattice volume fraction of 40% and 20%, with the predicted and observed periods listed. b) Schematic depiction of the location of the tracer point at the central node of the BCC unit cell and the path of the pressure wave along the unit cell diagonal.

To solve for U_p, we use a technique called graphical impedance matching in which we equate the interfacial pressures between the projectile and target as shown in Fig. 4-10, where pressure is given by the pressure-particle velocity relation (cf. Eq. 4.3). Considering that the projectile begins with the initial impact velocity V, we have to perform a change of coordinates by reflecting its curve about the y-axis and change its origin from 0 to V. After plotting the inverted pressure-particle velocity relation for the projectile and the known pressure-particle velocity relation for the target, U_p is simply the intersection of the two curves. Setting up this equality, where the projectile and target are referred to with subscripts 1 and 2, respectively, gives

$$\rho_2(C_2 + S_2U_{p2})U_{p2} = \rho_1\left[C_1 + S_1(V - U_{p2})\right](V - U_{p2}). \tag{4.4}$$

Inserting the shock parameters listed in Table 4.1 and an initial impact velocity of 1000 m/s and solving for U_{p2} in Eq. 4.4 gives a particle velocity in steel $U_{p2} = 0.50$ km/s.

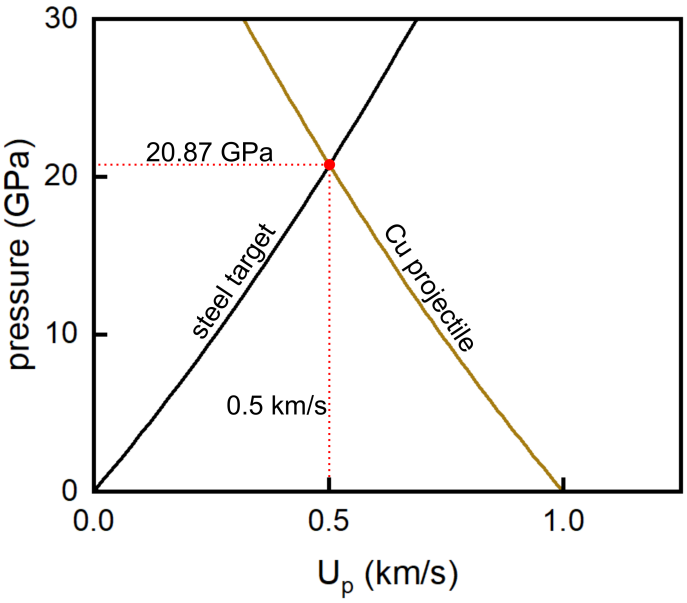

Figure 4-10: Graphical impedance matching for the copper projectile and the 316L stainless steel target based on Eq. 4.4, using shock parameters listed in table 4.1 and an impact velocity of 1 km/s.

Table 4.1: Shock parameters for copper, 316L stainless steel, and A356 aluminum.

material	$\boldsymbol{\rho}$ [g/cm^3]	$\boldsymbol{C_0}$ [km/s]	$\boldsymbol{S}$
copper	8.92	4.92	1.34
316L stainless steel	7.91	4.46	1.54
A356 aluminum	2.67	5.40	1.11

To calculate the initial peak pressure, we now plug the calculated $U_{p2} = 0.50$ km/s and the shock parameters of the steel target into Eq. 4.3, giving a predicted pressure of 20.87 GPa. This value agrees well with the observed initial peak pressure of 19.11 GPa shown in Fig. 4-9a, suggesting that this method can be used to reliably predict peak pressure. And while this impedance matching technique is most commonly used to evaluate shock behavior following plate impact of monolithic solids and laminates, it is likely accurate in evaluating the composites at hand due to the steady-wave behavior of the composite as discussed previously in Section 4.3. If the composite were to exhibit unsteady-wave behavior, invoking the pressure-particle velocity Hugoniot relation would likely only be accurate in predicting pressure very near to the strike face because the shock wave would continuously disperse as it travels into the composite, causing the pressure measured from the tracer point to deviate from its predicted equilibrium value. Note that by comparison, the pressure history in Fig. 4-9a is measured within the second unit cell in the composite, sufficiently far from the strike face, again indicating the steady-wave behavior of the composite. Furthermore, we note that in a composite with more unit cells in the shock direction—on the order of tens to hundreds—the pressure would likely decay due to spatial dissipation as energy from the shock wave is irreversibly deposited into the composite, and the pressure prediction would no longer be accurate. However, on the current length-scale of several unit cells, the steady-wave behavior holds and we can accurately predict the initial peak pressure by approximating the IPC as a laminated composite and inserting material properties.

As discussed previously, several aspects of the pressure response including oscillation period and initial peak can be predicted by locally approximating the composite as a laminate. However, we find that this approximation overestimates the post-shock mean pressure in our architectured IPCs [37], suggesting that the relative complexity of the internal mesoscale geometry causes these IPCs to attenuate shock more strongly than laminated composites of the same relative composition. We apply this treatment as follows, with the impactor and constituent materials denoted by subscripts 1, 2, and 3, respectively. The mean pressure σ_{mean} in laminated composites is

given analytically by

$$\sigma_{mean} = \frac{\tilde{\rho}_0 \tilde{U}_s \rho_1 U_{s1}}{\rho_1 U_{s1} + \tilde{\rho}_0 \tilde{U}_s} V \tag{4.5}$$

where $\tilde{\rho}_0$ is the density of the composite, given by a rule of mixtures, ρ_1 is the material density of the impactor, U_{s1} is the resulting shock velocity in the impactor, V is the impact velocity, and $\tilde{U}_s$ is the late-time velocity for shock loading, given by

$$\tilde{U}_s = \frac{h_2' + h_3'}{\sqrt{(\frac{h_2^0}{U_{s2}})^2 + (\frac{h_3^0}{U_{s3}})^2 + (R' + \frac{1}{R^0})\frac{h_2^0 h_3^0}{U_{s2} U_{s3}}}}, \tag{4.6}$$

with post-shock impedance ratio R' given by

$$R' = \frac{\rho_3' U_{s3}}{\rho_2' U_{s2}}, \tag{4.7}$$

post-shock material densities ρ_i'

$$\rho_i' = \left(\frac{1}{1 - \frac{U_{pi}}{U_{si}}} \right) \rho_i, \tag{4.8}$$

and similarly, layer thicknesses h_i'

$$h_i' = \left(\frac{1}{1 - \frac{U_{pi}}{U_{si}}} \right) h_i. \tag{4.9}$$

To solve for predicted mean pressure, we insert the shock parameters given in table 4.1, impact velocity V of 1000 m/s and layer thicknesses $h_2^0 = 1$ mm and $h_3^0 = 1.5$ mm for steel and Al, respectively. We can also solve for U_{p3} and U_{s3}, the particle velocity and shock velocities in Al, respectively, by using the impedance matching technique done previously for steel, giving $U_{p3} = 0.70$ km/s and $U_{s3} = 6.33$ km/s. Plugging these into Eq. 4.6-4.9 and solving Eq. 4.5 gives a predicted mean pressure σ_{mean} of 19.01 GPa. To find the actual post-shock mean pressure, we performed a Fourier transform on the oscillatory pressure history and recovered the zero-frequency value, as shown in Fig. 4-11b. The observed mean pressure is 14.93 GPa, which is much less than the mean pressure of 19.01 GPa predicted analytically for an analogous

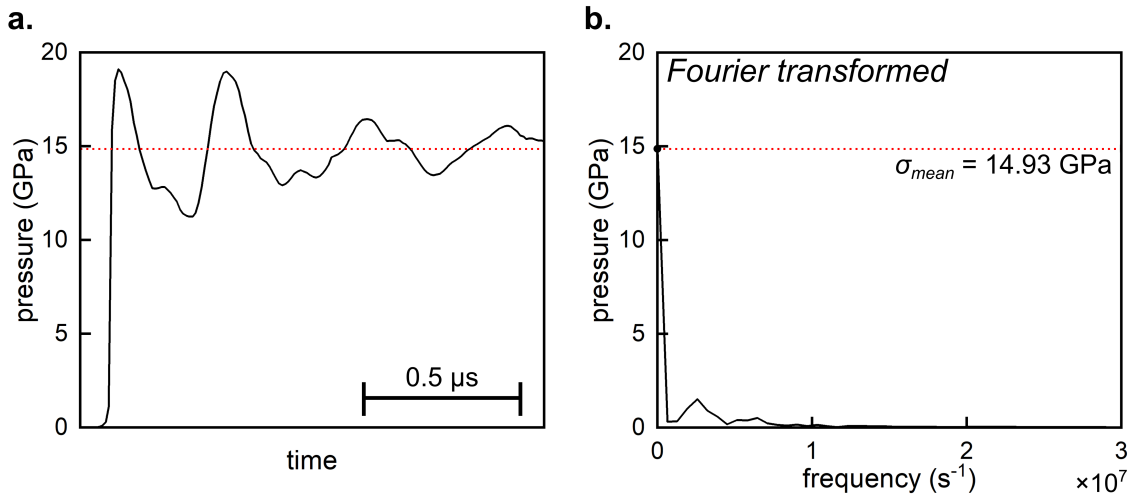

Figure 4-11: a) Pressure history for the tracer point located at the central node of the BCC unit cell for a lattice volume fraction of 40%. b) Fourier transform of the plot in Fig. 4-11a which reveals the mean pressure σ_{mean}.

laminated composite.

Next, we can link the oscillation period to the lattice geometry by considering the time-dependent pressure response to be the result of internal wave reflections within the composite. A similar approach was previously taken to predict the time-dependent pressure response within laminated composites [37], where the 1-D paths of individual wave trains were tracked between laminate layers by tracking interfacial reflections. Analogously, considering the 3-D IPCs at hand, we can roughly predict the period of the pressure oscillations by following the path of the shock wave along the unit cell diagonal. For lower lattice volume fractions, this multi-step path is shown schematically in Fig. 4-9b and is outlined sequentially in Fig. 4-12, where high-pressure regions of interest are traced. First, as shown in Fig. 4-12a, the shock front reaches the tracer point, resulting in the initial peak pressure. Next, shown in Fig. 4-12b, the pressure wave travels diagonally along the steel lattice strut towards the central node of the BCC unit cell. Once the pressure wave reaches the central node, shown in Fig. 4-12c, it is reflected by the interfaces where adjacent struts meet. The reflected wave then travels back through the original strut, shown in Fig. 4-12d, until it reaches the original tracer point, resulting in the next pressure peak (cf. Fig. 4-9). This process repeats as the wave is continuously reflected along the strut,

resulting in the oscillatory pressure response shown in Fig. 4-9a.

To analytically characterize the period of these wave reflections, we first find the shock velocity in the steel lattice struts using the shock velocity-particle velocity Hugoniot relation, given by

$$U_s = C_0 + SU_p. \tag{4.10}$$

From Eq. 4.10, we see that calculating the shock velocity within the steel requires first finding its particle velocity U_p. This calculation was performed earlier for steel using the impedance matching technique outlined in Eq. 4.4, resulting in $U_{p2} = 0.50$ km/s. Plugging this value into Eq. 4.10 along with characteristic shock parameters for steel as listed in Table 4.1 gives shock velocity $U_s = 5.24$ km/s in steel.

Using this shock velocity in steel, we can then predict the pressure oscillation period by following the path of the pressure wave through the steel lattice strut according to the sequence in Fig. 4-12. For the first half of this sequence (cf. Fig. 4-12a-c), using $U_s = 5.24$ km/s and a total unit cell length of 2.5 mm predicts that it takes 0.24 μs for the pressure wave to travel from the tracer point to the central node of the BCC lattice. For the remaining steps in the sequence in which the reflected pressure wave travels back through the lattice strut (cf. Fig. 4-12d-e), we have to consider that the material has been compressed by the initial passage of the shock wave. Accordingly, we can approximately reduce the distance by a factor $(1 - \frac{U_p}{U_s})$ which is used for monolithic material and laminated composites [37]. Performing a similar calculation for the second half of the sequence (cf. Fig. 4-12d-e) using $U_p = 0.50$ km/s and including the approximate distance reduction factor predicts a time for the entire sequence of 0.41 μs, which matches closely to the observed 0.35 μs shown in Fig. 4-9a for the first pressure oscillation period. Notably, this prediction depends only on the geometric parameters of the BCC unit cell, material properties, and impact velocity, and is independent of lattice volume fraction. This independence of the initial pressure oscillation period on lattice volume fraction is further shown by the near-identical first pressure oscillation period of 0.34 μs for a lattice volume fraction of 20%, as shown in the inset of Fig. 4-9a.

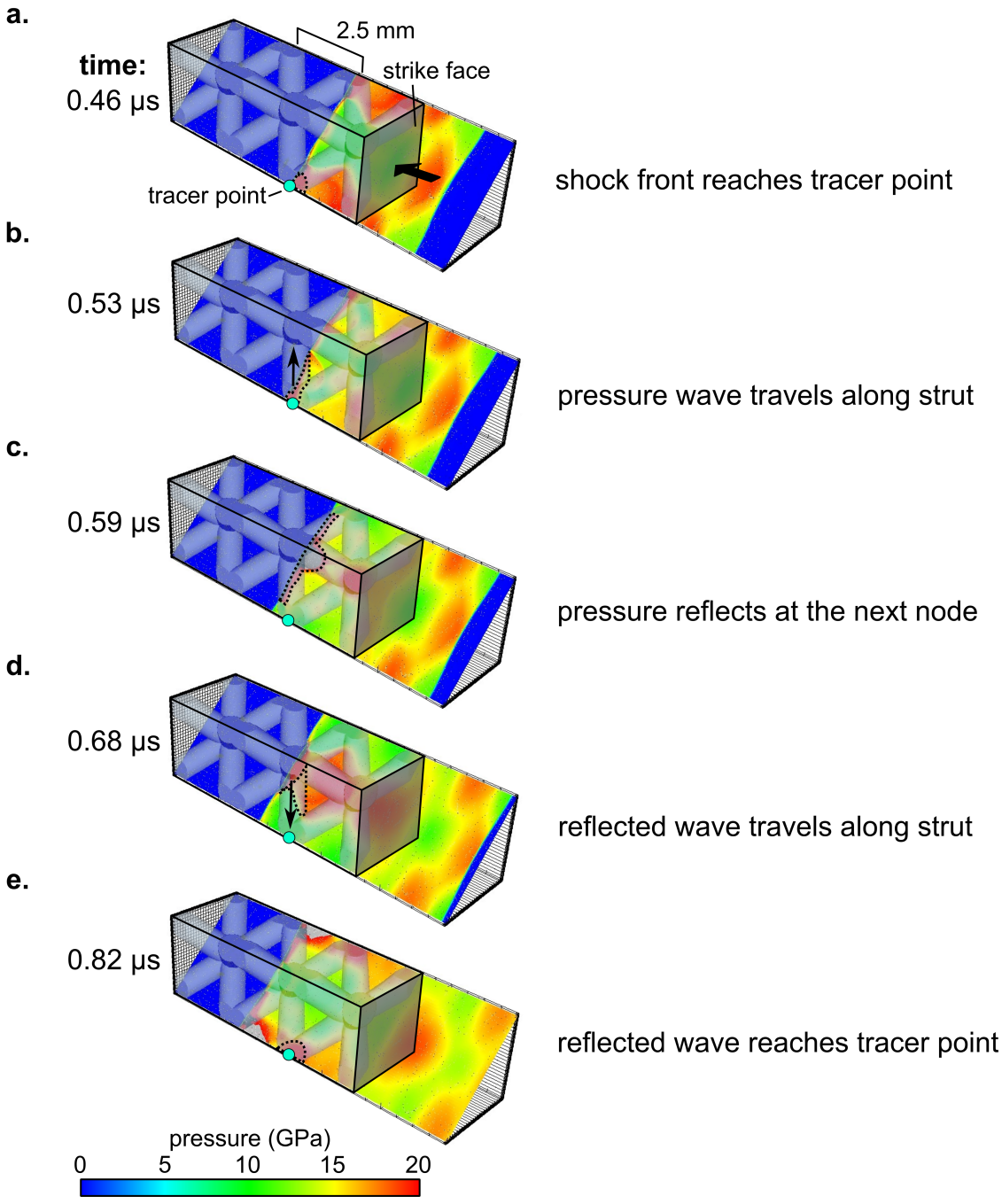

Figure 4-12: Pressure contour plot for 5 different time steps, showing the path of the pressure wave that results in an oscillatory pressure response measured from the tracer point shown.

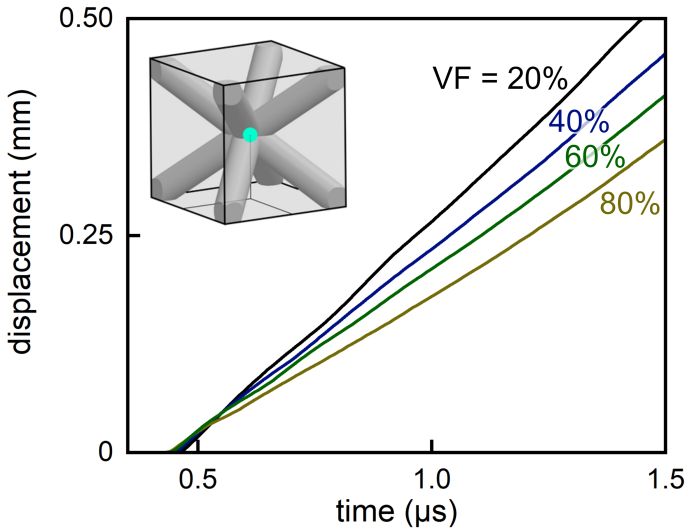

Figure 4-13: Longitudinal displacement history at a given tracer point for varying lattice volume fraction.

While the time between the first two peaks in the pressure response is independent of lattice volume fraction, we see that by comparison, the time between subsequent pressure peaks is shorter for the composite with a lattice volume fraction of 20%. Specifically, the oscillation periods between the subsequent pressure peaks from Fig. 4-9a are 0.21 μs and 45 μs for composites with 20% and 40% lattice volume fraction, respectively. The composites exhibit this difference in period because after the initial passage of the shock wave (cf. Fig. 4-12a-c), composites with lower lattice volume fraction, which in turn have less structural reinforcement, experience greater longitudinal compression. This trend is supported by Fig. 4-13, where the longitudinal displacement of the tracer point is greater for composites with lower lattice volume fraction. As a result of this greater longitudinal compression, the post-shock unit cell length is smaller, and the reflected pressure wave has a shorter distance to travel when returning to the tracer point, leading to a smaller subsequent period in the oscillations of the pressure response.

While the oscillatory pressure response of composites with low lattice volume fractions is dominated by reflections of pressure waves from node-to-node within the diagonal struts of the lattice (cf. Fig. 4-9b), the oscillatory pressure response for com-

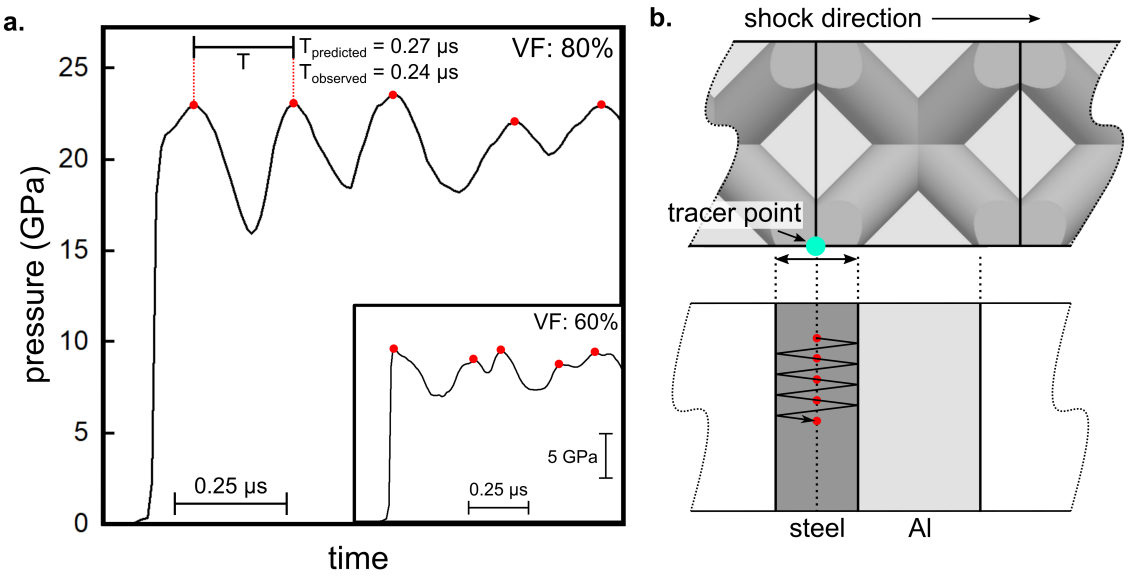

Figure 4-14: a) Pressure history for the tracer point located at the central node of the BCC unit cell for a lattice volume fraction of 80% and 60%, with the predicted and observed periods listed. b) Schematic depiction of the location of the tracer point at the central node of the BCC unit cell and the path of the pressure wave within the steel lattice strut.

posites with greater volume fractions, shown in Fig. 4-14a, is generally dominated by longitudinal pressure wave reflections within the node itself, as shown schematically in Fig. 4-14b. This behavior is most clearly exhibited by the composite with lattice volume fraction of 80%, where we can again more closely examine the oscillatory pressure response by following the reflections of the pressure wave. For the composite with lattice volume fraction of 80%, the total width of the node is 1.62 mm; using the previously calculated shock velocity $U_s = 5.24$ km/s and particle velocity $U_{p2} = 0.50$ km/s, and considering the approximate post-shock compression factor $(1 - \frac{U_p}{U_s})$, we predict that the pressure wave returns to the tracer point in 0.27 μs. This predicted value matches closely with the observed pressure oscillation period of 0.24 μs, indicating that the pressure response for composites with greater lattice volume fractions is dominated by longitudinal motion, similar to that of laminated composites.

By comparison, the pressure response of the composite with lattice volume fraction

of 60%, shown in the inset of Fig. 4-14a, is irregular. This irregularity in peak timing is likely the result of a mixed-mode type of behavior, where the pressure response is a combination of pressure waves reflected both along the unit cell diagonal and longitudinally within the node (cf. Fig. 4-9b and Fig. 4-14b, respectively). Considering this mixed-mode behavior in the pressure response of the composite with lattice volume fraction of 60%, we predict that a transition in behavior occurs in composites with intermediate lattice volume fractions. Notably, we see clear evidence of this mixed-mode behavior and transition in the pressure response of the composite with 40% lattice volume fraction, where the secondary peaks marked by blue dots in Fig. 4-9a are well discernible from the larger peaks of the dominant pressure response. We can predict the timing of these secondary peaks by tracking longitudinal pressure wave reflections within the node, similar to the process done earlier for the composite with lattice volume fraction of 80%. Using the same shock parameters for steel—shock velocity $U_s = 5.24$ km/s, particle velocity $U_{p2} = 0.50$ km/s, and approximate post-shock compression factor $(1-\frac{U_p}{U_s})$—with a node width of 0.98 mm, we predict that the pressure wave will return to the tracer point in 0.17 μs, which matches closely with the period of 0.15 μs for the secondary pressure peaks. Thus, although the pressure response of the composite with 40% volume fraction is dominated by pressure wave reflections along the diagonal of the BCC unit cell, we observe slight mixed-mode behavior, where secondary peaks are the result of pressure wave reflections in the longitudinal direction. We also note that these secondary peaks are not present in the pressure response of the composite with 20% volume fraction. The transition in behavior thus begins between 20% and 40% volume fraction, likely when the surface area of the interface between the steel node and the Al matrix becomes large enough to cause appreciable reflection of the pressure wave in the longitudinal direction.

While the behavior of the pressure response is independent of lattice volume fraction at low percents (i.e., with lattice volume fraction of 40% and below), the longitudinal velocity response, V_L, shown in Fig. 4-15a, is solely dependent on lattice volume fraction and is dominated by longitudinally reflected waves within the node as shown schematically in Fig. 4-15b. Thus, for composites of varying lattice volume fractions,

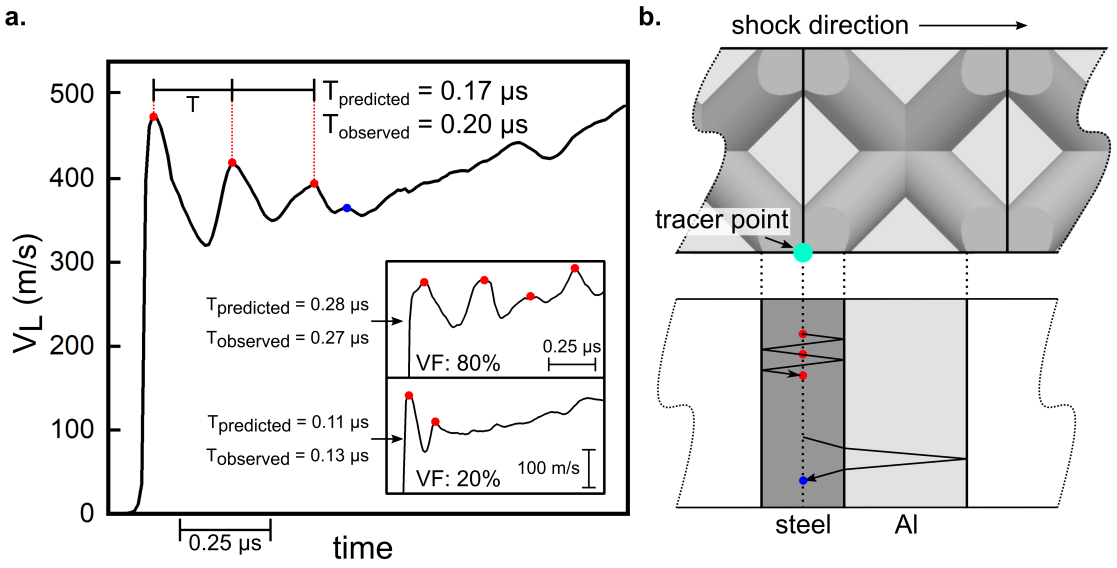

Figure 4-15: (a) Longitudinal velocity history with lattice volume fraction of 40% (with 80% and 20% inset). Predicted and observed oscillation period are listed. (b) Representation of the shock wave reflection history at the given tracer point location.

we can closely predict the V_L oscillation periods as given in Fig. 4-15a by treating the IPC as a laminated composite in the vicinity of the tracer point at the central node of the BCC lattice and tracking the reflections of the shock wave within the node as done previously for the pressure response at higher volume fractions. Accordingly, we treat the IPC as a laminated composite with geometric parameters listed in table 4.2, using shock parameters from table 4.1 and constituent shock velocities and particle velocities as calculated earlier. The resulting predicted and observed V_L oscillation periods are summarized in table 4.2 and show good agreement, indicating that the longitudinal velocity response is dominated by the longitudinal reflection behavior within the node (cf. Fig. 4-15a). We note that the V_L period decreases with decreasing lattice volume fraction as expected by geometry, where thinner layers within a laminated composite result in a shorter distance for the wave to travel before returning to the tracer point. Notably, a similar effect was observed in laminated composites, where decreasing layer thickness resulted in a smaller V_L oscillation period [6]. This similarity in behavior further suggests that the V_L response can be accurately predicted by locally approximating the IPC as a laminated composite.

We also observe that this predictable, oscillatory behavior in V_L ends after several

Table 4.2: Parameters used to approximate the IPCs of varying lattice volume fractions as laminated composites, and the resulting predicted vs. observed V_L period.

volume fraction	**steel thickness** [mm]	**Al thickness** [mm]	**predicted period** [μs]	**observed period** [μs]
20%	0.65	1.85	0.11	0.13
40%	0.98	1.52	0.17	0.20
80%	1.62	0.88	0.28	0.27

cycles, after which the oscillations cease and V_L approaches an equilibrium value. This process is shown beginning at the blue point in Fig. 4-15a and can be predicted by approximating the time at which the shock wave reflects from the subsequent steel/Al interface at the next lattice strut, as shown schematically in Fig. 4-15b. In particular for the composite with lattice volume fraction of 40%, we can use the previously applied procedure to follow the shock wave through this path. Following the same process while using constituent shock and particle velocities as previously calculated predicts that the V_L response will begin to homogenize 0.60 μs after the initial arrival of the shock front at the tracer point, which agrees well with the observed 0.56 μs. Furthermore, the equilibrium V_L value can be accurately estimated using the impedance matching technique applied previously, where the predicted 501.4 m/s agrees closely with the 508.9 m/s observed at the end of the measuring period.

4.4.2 Orientation Dependence

While the macroscale shock velocity-particle velocity relation is independent of orientation, as described in Section 4.3, we see that several aspects of the fine-scale shock response depend on impact orientation. For instance, the oscillatory nature of the longitudinal velocity histories for the [100], [110], and [111] orientations are shown in Fig. 4-16, again measured from the tracer point at the central node of the BCC lattice as shown in the inset figure. As previously discussed, the longitudinal velocity history of the [100] orientation is oscillatory in nature due to longitudinal wave reflections within the node. By comparison, the time in between peaks of the longitudinal velocity history of the [110] orientation is greater because in the [110]

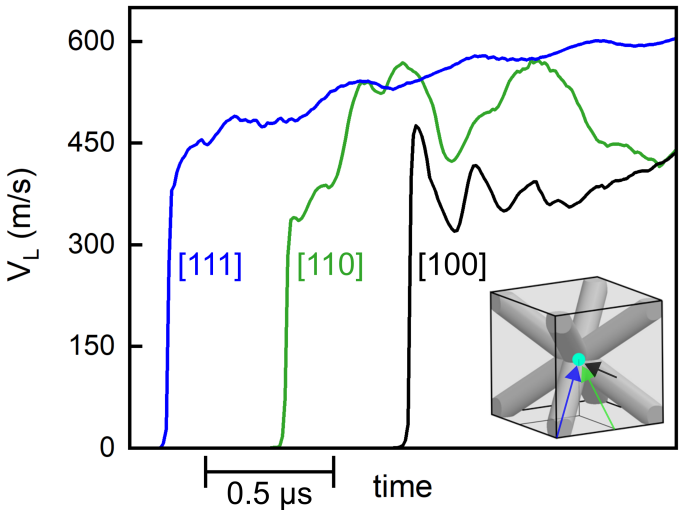

Figure 4-16: Longitudinal velocity history with varying impact orientation.

orientation, where the unit cell is effectively rotated 45°, the nodes of the lattice are spaced further apart, causing less frequent internal wave reflections. And notably, the longitudinal velocity history of the [111] is nearly absent of oscillatory behavior by the same mechanism, where in the [111] orientation, the path of the shock wave along the tracer point at the central node lies within the diagonal strut of the BCC lattice. As a result, the propagating shock wave encounters no steel/Al interfaces, and the tracer point records no strongly reflected waves. This linkage between impact orientation and longitudinal velocity history further suggests that the fine-scale shock response, and the oscillatory behavior of the longitudinal velocity history, is the result of internal wave reflections at interfaces within the composite.

Furthermore, we observe that impact orientation has a strong effect on the spread of the shock front and the resulting shock front width. The pressure histories for a given tracer point for the [110] and [111] orientations are shown in Fig. 4-17. Using Eq. 4.2, the shock front widths of the [110] and [111] impact orientations are 0.41 mm and 0.85 mm, respectively, as compared to the 1.04 mm shock front width of the [100] impact orientation as discussed in Section 4.3. The shock front width of

the [100] impact orientation is greatest due to the openness of the structure as shown in Fig. 4-3 which causes the shock front to split into regimes of two distinct velocities based on position. Though to a lesser extent, the shock front widens in the [111] impact orientation due to the relative internal complexity of the structure and its high concentration of internal interfaces. As a result, the shock front encounters many interfaces during propagation, leading to numerous multiple-wave interactions and shock redirections that spread the shock wave in a less predictable manner than in the [100] impact orientation. This nonuniform behavior is shown by the relative spreading of the shock front within both the steel and Al in Fig. 4-17b. However, we also notably observe large peaks in the pressure histories of the steel tracer points in the [111] impact direction, likely due to the diagonal lattice struts which allow the shock front to propagate without encountering any interfaces as discussed previously. Nevertheless, these peaks show a relatively large spread, indicating nonuniform spreading of the shock front. By contrast, the histories of the steel and Al in the [110] direction are relatively uniform with little spacing between pressure histories of individual tracer points within Fig. 4-17a, indicating that the shock front has experienced relatively little spread within each constituent. This relatively tight shock front in the [110] impact orientation is the result of both the relative simplicity of the lattice in the [110] direction and the lack of openness in the structure, which leads to a relatively homogeneous shock front. And notably in both the [110] and [111] impact orientations, the shock front reaches tracer points within the Al before those within the steel for two reasons. First, the shock velocity in the Al is greater than that in the steel, where the shock velocities previously calculated by Eq. 4.10 are 5.24 km/s and 6.33 km/s in the steel and Al, respectively. And second, the shock wave is redirected within the steel lattice struts as discussed in Section 4.3, such that within a given plane, the shock wave must generally travel a greater distance before arriving at tracer points within the steel lattice.

Finally, we observe that the temperature response is also highly dependent upon impact orientation. Notably, we see that the maximum temperature increases with the openness of the structure, as shown in Fig. 4-18. Due to the open channels within

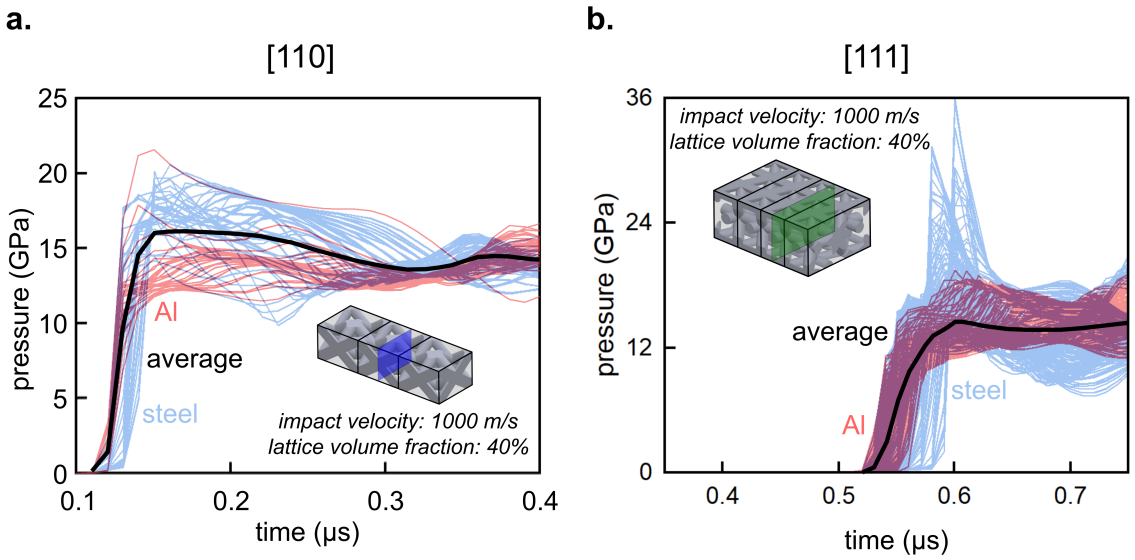

Figure 4-17: Pressure histories for tracer points at a given plane in the (a) [110] and (b) [111] impact orientations, with plane averages overlaid.

the [100] impact orientation, which cause a relatively large differential in shock speed within the Al phase, as discussed previously (cf. Fig. 4-4), the Al phase experiences large amounts of strain-induced heating and thus experiences the greatest maximum temperature of the three impact orientations. By comparison, the [110] impact orientation experiences slightly less strain-induced heating due to the lack of open channels within the structure and the relatively homogeneous shock front as shown in Fig. 4-17a. Similarly, the [111] impact orientation experiences a relatively low maximum temperature due to its high interfacial density which prevents shock velocity gradients from forming within the Al phase, thus reducing strain-induced heating within the Al. Interestingly, regardless of orientation, the maximum temperature occurs at interfaces parallel to the shock direction. At these interfaces, mechanical contact between the steel and Al phases limits longitudinal motion relative to more unrestricted regions further from these interfaces, leading to intraphase straining and heating.

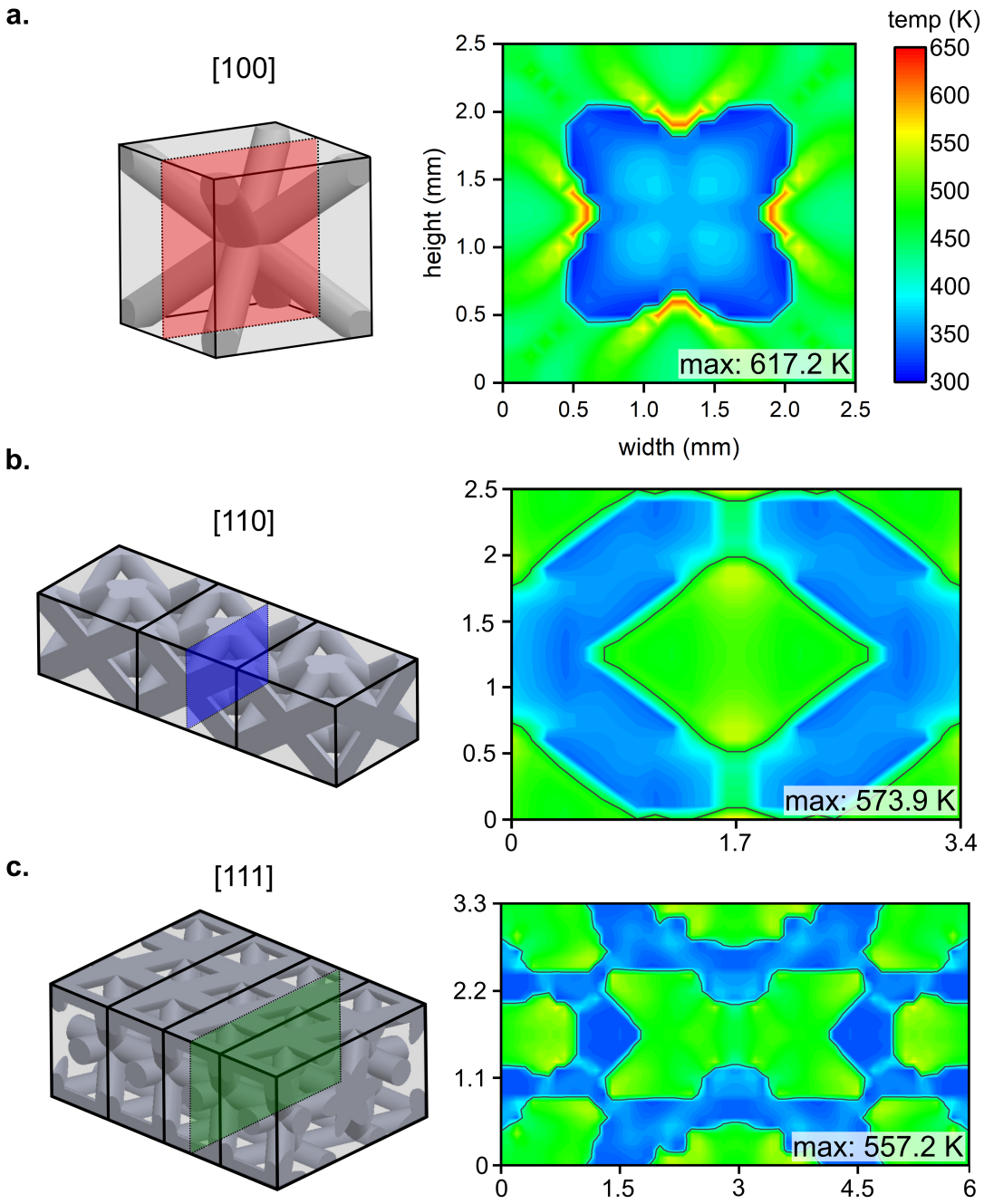

Figure 4-18: Temperature at the shock front for the [100], [110], and [111] orientations, measured from a given plane in the center of the unit cell. Steel and Al interfaces are outlined in black.

4.5 Summary

Motivated by the preliminary findings of previous studies, which indicate that the internal geometry of complex IPCs enhances shock viscosity, we further explore the relationship between mesoscale geometry and shock response of steel-Al IPCs through plate impact simulations with varying impact orientation and lattice volume fraction. In the macroscale, the shock velocity-particle velocity Hugoniot relation is independent of impact orientation and lies slightly below the kinetic-energy-average prediction, indicating that the internal geometry slows and spreads shock relative to its monolithic constituents. This shock viscosity is explained in part by the variation in the openness within the structure, which results in a shock front width on the length-scale of the unit cell. Finally, we observe that the angling of the lattice struts redirects some of the shock momentum into transverse motion, which acts as an additional method of shock dissipation and enhances macroscale shock viscosity.

In the fine-scale, we observe that the pressure and longitudinal velocity responses, measured from a tracer point at the center of the unit cell, are oscillatory in nature. We can analytically relate these oscillation periods to geometric features of the unit cell, such as the strut length and diameter, which gives an initial link between mesoscale geometry and shock response in these complex IPCs. We can predict other aspects of the pressure response, including maximum pressure, by using an impedance matching technique. Additionally, the temperature response depends on the openness of the structure, and hotspots appear at interfaces parallel to the impact direction. These structure-property linkages in architectured 3-D-printed IPCs will help advance the tailorability of their shock response, which can make them useful for a broad range of structural aerospace components and reactive systems.

Chapter 5

Conclusions and Future Work

Using additive manufacturing (AM), we can finely control the mesoscale geometry and the resulting mechanical properties of novel interpenetrating phase composites (IPCs), allowing us to extend their capabilities beyond those of their monolithic constituents. This ability to tailor mechanical properties makes 3-D-printable IPCs attractive for use in extreme aerospace environments, where in particular, tensile damage tolerance and shock resistance are often limiting properties for structural components. However, despite these potential merits, the linkage between such enabling mechanical properties and the mesoscale geometry of IPCs is currently not well understood. In this work, we developed initial linkages between mesoscale geometry and mechanical behavior by studying both the quasi-static tensile energy absorption and the shock response of 3-D printable architectured IPCs.

First, we studied the effects of geometry on the quasi-static tensile energy absorption behavior of a novel, 3-D-printable IPC called the chain lattice, which comprises a fully-dense reinforcement phase and a cellular filler material. In tension, these phases act together to delocalize damage and thereby improve strain-to-failure and specific energy absorption, similar to the composite effects seen in traditional brittle-matrix composites. The conclusions from this study are as follows:

1. The concept of the chain lattice was introduced, and key geometric parameters of the chain reinforcement and filler material were defined.

2. A delocalized damage criterion was developed, which considers geometric parameters of the chain reinforcement and filler material to predict the maximum filler material relative density that can enable damage delocalization.

3. Estimations for the tensile strain-to-failure and specific energy absorption of the chain lattice were developed based on geometric parameters of the chain reinforcement and the filler material.

4. Chain lattices with varying filler material relative density and constant chain reinforcement geometric parameters were 3-D printed from a photocurable poly(methyl methacrylate) resin and tested in tension.

5. The chain lattices exhibited a transition from delocalized to localized damage behavior at a filler material relative density that was accurately predicted by the delocalized damage criterion.

6. In the chain lattice which exhibited the most ideal damage behavior, the measured strain-to-failure and specific energy absorption agree well with those predicted by the analytical models.

7. Using the validated models, we predict that a chain lattice printed from an ideally brittle ceramic material can exhibit a tensile specific energy absorption roughly more than an order-of-magnitude greater than that of its monolithic parent material.

Beyond this initial demonstration, the chain lattice can be specifically customized to broaden its range of capabilities. For example, while the present work focuses on 1-D chain lattices, chain lattices can be extended to higher dimensions for multi-axial damage tolerance by incorporating 2-D or 3-D chainmail reinforcements. Additionally, we can further tailor chain lattice failure mechanisms and energy absorption characteristics by incorporating alternative lattice structures such as shell lattices [59] and honeycombs [60]. By leveraging the control over form and fine-scale printability offered by AM, chain lattices can be directly printed into complex net-shapes

and can incorporate functional gradients in lattice architecture which allow for optimal, site-specific properties at even micro- and nanoscale resolution. And finally, novel AM techniques such as projection microstereolithography of preceramic polymers and two-photon lithography with atomic layer deposition have been used to form ceramic microlattices and nanolattices [61, 62], where these small length-scales improve strength according to Weibull statistics for brittle materials [63]; such advanced AM techniques can thus be used to fabricate micro- and nanoscale chain lattices, enabling corresponding strength improvements. These different capabilities, considered together, indicate that the hierarchical architecture of the chain lattice can impart brittle 3-D-printable materials with enhanced damage-tolerance and energy absorption in tension.

Next, we studied the shock response of an IPC comprised of a steel body-centered cubic (BCC) lattice embedded in an aluminum matrix. This IPC construction is of interest, in part, because the relative difference in constituent shock impedance gives rise to interesting composite shock phenomena. Furthermore, the quasi-static mechanical properties of these steel-Al IPCs have been well studied, and they can be reliably manufactured [13, 44]. Our shock dynamics study led to the following conclusions:

1. Plate impact simulations were performed on steel-Al IPCs with varying impact velocity, lattice volume fraction, and impact orientation.

2. In the macroscale, the shock velocity-particle velocity Hugoniot relation lies slightly below that of the kinetic energy average of its monolithic constituents, is independent of impact orientation, and decreases linearly with lattice volume fraction.

3. Due to the openness of the structure in the [100] impact orientation, the shock velocity varies by location and the shock front spreads as it propagates into the composite.

4. Shock transfer and reflection at oblique lattice interfaces convert a fraction of the longitudinal shock velocity into transverse motion.

5. On the length-scale of several unit cells, the periodicity of the mesoscale composite geometry supports a steady shock wave.

6. The fine-scale pressure and longitudinal velocity histories are oscillatory in nature, where the oscillations result from interfacial wave reflections.

7. Structural openness increases strain-induced heating, which causes high-temperature hotspots at interfaces parallel to the shock direction.

This shock dynamics study will be continued, first, with experimental plate impact tests which will serve to validate these findings from simulations. Preliminary infiltrated BCC preforms are shown in Fig. 5-1, from which plate impact specimens will be machined and tested. Beyond experimental validation, the initial findings in this work call for further investigation in several key areas. For instance, we can form these architecured IPCs from a wide variety of material combinations to gauge the effect of material properties, such as shock impedance mismatch, on the composite shock response. More complex lattice geometries, such as octet-truss lattices, triply-periodic minimal surfaces, and lattice structures with functional gradients, can further elucidate the relationship between mesoscale geometry and shock response. Finally, considering the hotspot formation in these simple BCC structures, we can further tailor the mesoscale geometry to induce hotspots at specific, desired points within the lattice. The ability to control hotspot formation has strong implications for structural reactive systems such as munitions casings, which currently rely on stochastic post-shock pressure and temperature fields to drive reactions.

We can also use these initial findings to develop protective coatings for rocket engine components, which experience extreme heat and pressure cycling under high oxygen pressure. In these extreme conditions, thermal barrier coatings are often the only form of protection for critical rocket engine components, and as a result, are often a critical point of failure, where any flaking or melting of the coating can cause combustion of the underlying metal component and failure of the engine as a whole. Traditional thermal barrier coatings are particularly susceptible to mechanical damage, which is often induced by high-velocity impact of micrometeoroid and orbital

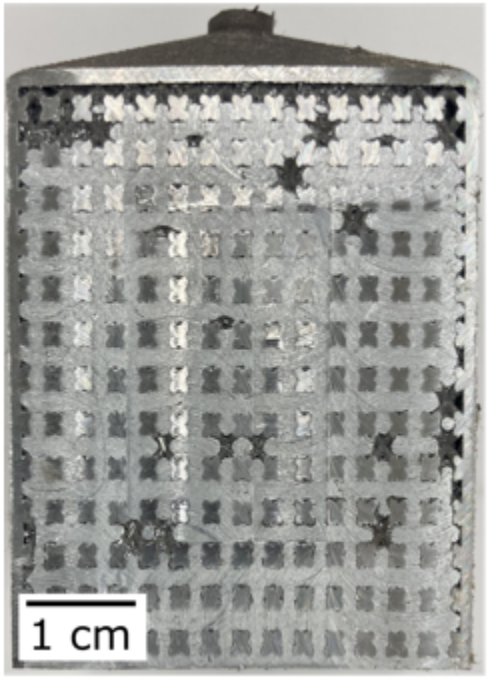

Figure 5-1: Open-faced infiltrated BCC preform.

debris [2]. With this current limitation in mind, the findings from this study motivate future work focused on a reemerging class of coatings made from interpenetrating phases, where the interpenetrating nature of the coating improves its mechanical bond strength and enhances its shock resistance through the geometry-dependent mechanisms observed in the IPCs in the current work.

Bibliography

[1] Frank W Zok. Ceramic-matrix composites enable revolutionary gains in turbine engine efficiency. *American Ceramic Society Bulletin*, 95(5):7.

[2] G. I. Zagainov and G. E. Lozino-Lozinsky, editors. *Composite Materials in Aerospace Design*. Springer Netherlands, Dordrecht, 1996.

[3] M.M. Stack, F.H. Stott, and G.C. Wood. Review of mechanisms of erosion-corrosion of alloys at elevated temperatures. *Wear*, 162-164:706–712, April 1993.

[4] Tim J Carter. Common failures in gas turbine blades. *Engineering Failure Analysis*, 12(2):237–247, April 2005.

[5] E. Grossman, I. Gouzman, and R. Verker. Debris/Micrometeoroid Impacts and Synergistic Effects on Spacecraft Materials. *MRS Bulletin*, 35(1):41–47, January 2010.

[6] Shiming Zhuang, Guruswami Ravichandran, and Dennis E. Grady. An experimental investigation of shock wave propagation in periodically layered composites. *Journal of the Mechanics and Physics of Solids*, 51(2):245–265, February 2003.

[7] T.J. Vogler, M.Y. Lee, and D.E. Grady. Static and dynamic compaction of ceramic powders. *International Journal of Solids and Structures*, 44(2):636–658, January 2007.

[8] Michael A. Mattoni, James Y. Yang, Carlos G. Levi, and Frank W. Zok. Effects of Matrix Porosity on the Mechanical Properties of a Porous-Matrix, All-Oxide Ceramic Composite. *Journal of the American Ceramic Society*, 84(11):2594–2602, November 2001.

[9] D Horvitz, I Gotman, E.Y Gutmanas, and N Claussen. In situ processing of dense Al2O3–Ti aluminide interpenetrating phase composites. *Journal of the European Ceramic Society*, 22(6):947–954, June 2002.

[10] C. San Marchi, M. Kouzeli, R. Rao, J.A. Lewis, and D.C. Dunand. Alumina–aluminum interpenetrating-phase composites with three-dimensional periodic architecture. *Scripta Materialia*, 49(9):861–866, November 2003.

[11] L.D Wegner and L.J Gibson. The fracture toughness behaviour of interpenetrating phase composites. *International Journal of Mechanical Sciences*, 43(8):1771–1791, August 2001.

[12] L.D. Wegner and L.J. Gibson. The mechanical behaviour of interpenetrating phase composites – II: a case study of a three-dimensionally printed material. *International Journal of Mechanical Sciences*, 42(5):943–964, May 2000.

[13] Alexander E. Pawlowski, Zachary C. Cordero, Matthew R. French, Thomas R. Muth, J. Keith Carver, Ralph B. Dinwiddie, Amelia M. Elliott, Amit Shyam, and Derek A. Splitter. Damage-tolerant metallic composites via melt infiltration of additively manufactured preforms. *Materials & Design*, 127:346–351, August 2017.

[14] Benjamin C White, Anthony Garland, Ryan Alberdi, and Brad L. Boyce. Interpenetrating Lattices with Enhanced Mechanical Functionality. *Additive Manufacturing*, 38:101741, 2021.

[15] I. Song and N. N. Thadhani. Shock-induced chemical reactions and synthesis of nickel aluminides. *Metallurgical Transactions A*, 23(1):41–48, January 1992.

[16] Naresh N. Thadhani. Shock-induced chemical reactions and synthesis of materials. *Progress in Materials Science*, 37(2):117–226, January 1993.

[17] Kyle T. Sullivan, Cheng Zhu, Eric B. Duoss, Alexander E. Gash, David B. Kolesky, Joshua D. Kuntz, Jennifer A. Lewis, and Christopher M. Spadaccini. Controlling Material Reactivity Using Architecture. *Advanced Materials*, 28(10):1934–1939, March 2016.

[18] A. G. Evans and F. W. Zok. The physics and mechanics of fibre-reinforced brittle matrix composites. *Journal of Materials Science*, 29(15):3857–3896, 1994.

[19] J. A. DiCarlo, H M. Yun, G. N. Morscher, and R. T. Bhatt. SiC/SiC Composites for 1200°C and Above. In Narottam P. Bansal, editor, *Handbook of Ceramic Composites*, pages 77–98. Springer US, 2005.

[20] John C. McNulty, Frank W. Zok, Guy M. Genin, and Anthony G. Evans. Notch-Sensitivity of Fiber-Reinforced Ceramic-Matrix Composites: Effects of Inelastic Straining and Volume-Dependent Strength. *Journal of the American Ceramic Society*, 82(5):1217–1228, December 2004.

[21] S.J. Connell, F.W. Zok, Z.Z. Du, and Z. Suo. On the tensile properties of a fiber reinforced titanium matrix composite—II. Influence of notches and holes. *Acta Metallurgica et Materialia*, 42(10):3451–3461, October 1994.

[22] Carl Cady, Fernando E. Heredia, and Anthony G. Evans. In-Plane Mechanical Properties of Several Ceramic-Matrix Composites. *Journal of the American Ceramic Society*, 78(8):2065–2078, August 1995.

[23] Brian N. Cox, Mahyar S. Dadkhah, and W.L. Morris. On the tensile failure of 3D woven composites. *Composites Part A: Applied Science and Manufacturing*, 27(6):447–458, January 1996.

[24] B.N. Cox, J.B. Davis, N. Sridhar, F. W. Zok, and X.-Y. Gong. Designing Composites for Energy Absorption Under Tensile Loading. *Proceedings of the 1999 International Conference on Composite Materials*, page 10, 1999.

[25] Anne-Marie Harte, Norman A. Fleck, and Michael F. Ashby. Energy absorption of foam-filled circular tubes with braided composite walls. *European Journal of Mechanics - A/Solids*, 19(1):31–50, January 2000.

[26] X.Y. Gong, F.W. Zok, B.N. Cox, and J. Davis. The mechanics of delocalization and energy absorption in chain composites. *Acta Materialia*, 48(3):745–753, February 2000.

[27] B.N. Cox, N. Sridhar, J.B. Davis, X.-Y. Gong, and F.W. Zok. The energy absorption potential of chain composites. *Acta Materialia*, 48(3):755–766, February 2000.

[28] B N Cox. Lockup, chains and the delocalization of damage. *Journal of Materials Science*, 30:4871–4881, 1995.

[29] L.J. Gibson and M. F. Ashby. *Cellular Solids*. Cambridge Solid State Science Series. Cambridge University Press, 2 edition, 1999.

[30] V.S. Deshpande, M.F. Ashby, and N.A. Fleck. Foam topology: bending versus stretching dominated architectures. *Acta Materialia*, 49(6):1035–1040, April 2001.

[31] M.F Ashby. The properties of foams and lattices. *Philosophical Transactions of the Royal Society A: Mathematical, Physical and Engineering Sciences*, 364(1838):15–30, January 2006.

[32] L. M. Barker. Laser interferometry in shock-wave research: Author reviews the various types of interferometer that have been applied to shock-wave research and describes the present capabilities and limitations. *Experimental Mechanics*, 12(5):209–215, May 1972.

[33] Dennis E. Grady. Structured shock waves and the fourth-power law. *Journal of Applied Physics*, 107(1):013506, January 2010.

[34] William Band and George E. Duvall. Physical Nature of Shock Propagation. *American Journal of Physics*, 29(11):780–785, November 1961.

[35] Stanley Marsh. LASL Shock Hugoniot Data, 1980.

[36] Marc A. Meyers. *Dynamic behavior of materials*. Wiley, New York, 1994.

[37] X. Chen, N. Chandra, and A.M. Rajendran. Analytical solution to the plate impact problem of layered heterogeneous material systems. *International Journal of Solids and Structures*, 41(16-17):4635–4659, August 2004.

[38] Paul E. Specht, Naresh N. Thadhani, and Timothy P. Weihs. Configurational effects on shock wave propagation in Ni-Al multilayer composites. *Journal of Applied Physics*, 111(7):073527, April 2012.

[39] Paul E. Specht, Timothy P. Weihs, and Naresh N. Thadhani. Interfacial Effects on the Dispersion and Dissipation of Shock Waves in Ni/Al Multilayer Composites. *Journal of Dynamic Behavior of Materials*, 2(4):500–510, December 2016.

[40] John P. Borg and Tracy J. Vogler. Mesoscale calculations of the dynamic behavior of a granular ceramic. *International Journal of Solids and Structures*, 45(6):1676–1696, March 2008.

[41] T. J. Vogler, J. P. Borg, and D. E. Grady. On the scaling of steady structured waves in heterogeneous materials. *Journal of Applied Physics*, 112(12):123507, December 2012.

[42] Vitali F. Nesterenko. *Dynamics of Heterogeneous Materials*. Springer New York, New York, NY, 2001.

[43] Abdel R. Moustafa, Ralph B. Dinwiddie, Alexander E. Pawlowski, Derek A. Splitter, Amit Shyam, and Zachary C. Cordero. Mesostructure and porosity effects on the thermal conductivity of additively manufactured interpenetrating phase composites. *Additive Manufacturing*, 22:223–229, August 2018.

[44] Jiahao Cheng, Maxim Gussev, Jason Allen, Xiaohua Hu, Abdel R. Moustafa, Derek A. Splitter, and Amit Shyam. Deformation and failure of PrintCast A356/316 L composites: Digital image correlation and finite element modeling. *Materials & Design*, 195:109061, October 2020.

[45] Lauren L Poole, Manny Gonzales, Matthew R French, William A Yarberry Iii, and Zachary C Cordero. Hypervelocity Impact of PrintCast A356/316L Composites. 15:10, 2019.

[46] Lauren L Poole, Manny Gonzales, Abdel R. Moustafa, and Zachary C. Cordero. Shock Dynamics in Periodic Two-Dimensional Composites, 2020.

[47] Spencer V Taylor, Abdel R Moustafa, and Zachary C Cordero. Interpenetrating Lattices with Tailorable Energy Absorption in Tension. *Acta Materialia*, 216:117115, September 2021.

[48] George D. Quinn. Weibull Strength Scaling for Standardized Rectangular Flexure Specimens. *Journal of the American Ceramic Society*, 86(3):508–510, March 2003.

[49] Hamza Alsalla, Liang Hao, and Christopher Smith. Fracture toughness and tensile strength of 316L stainless steel cellular lattice structures manufactured using the selective laser melting technique. *Materials Science and Engineering: A*, 669:1–6, July 2016.

[50] C. I. Hammetter and F. W. Zok. Compressive Response of Pyramidal Lattices Embedded in Foams. *Journal of Applied Mechanics*, 81(1):011006, August 2013.

[51] Jaroslav Kováčik, Liviu Marsavina, and Emanoil Linul. Poisson's Ratio of Closed-Cell Aluminium Foams. *Materials*, 11(10):1–11, October 2018.

[52] Mark R. O'Masta, Ekaterina Stonkevitch, Kayleigh A. Porter, Phuong P. Bui, Zak C. Eckel, and Tobias A. Schaedler. Additive manufacturing of polymer-derived ceramic matrix composites. *Journal of the American Ceramic Society*, pages 1–12, June 2020.

[53] Anthony G. Evans, J.-M. Domergue, and E. Vagaggini. Methodology for Relating the Tensile Constitutive Behavior of Ceramic-Matrix Composites to Constituent Properties. *Journal of the American Ceramic Society*, 77(6):1425–1435, June 1994.

[54] Oren E. Petel and Francois X. Jetté. Comparison of methods for calculating the shock hugoniot of mixtures. *Shock Waves*, 20(1):73–83, February 2010.

[55] S.S. Batsanov. Synthesis and modification of materials by shock waves: real-time measurements and mechanisms of reaction. *Materials Science and Engineering: A*, 210(1-2):57–63, June 1996.

[56] R. S. Hixson, R. G. McQueen, and J. N. Fritz. The shock Hugoniot of 316 SS and sound velocity measurements. In *AIP Conference Proceedings*, volume 309, pages 105–108, Colorado Springs, Colorado (USA), 1994. AIP. ISSN: 0094243X.

[57] Neil K. Bourne. On the Shock Response of Polymers to Extreme Loading. *Journal of Dynamic Behavior of Materials*, 2(1):33–42, March 2016.

[58] W.J. Carter and S.P. Marsh. Hugoniot equation of state of polymers. Technical Report LA–13006-MS, 95183, July 1995.

[59] Xueyan Chen, Qingxiang Ji, Jianzheng Wei, Huifeng Tan, Jianxin Yu, Pengfei Zhang, Vincent Laude, and Muamer Kadic. Light-weight shell-lattice metamaterials for mechanical shock absorption. *International Journal of Mechanical Sciences*, 169:105288, March 2020.

[60] Douglas T. Queheillalt, Yasushi Katsumura, and Haydn N.G. Wadley. Synthesis of stochastic open cell Ni-based foams. *Scripta Materialia*, 50(3):313–317, February 2004.

[61] Xiaoyu Zheng, Howon Lee, Todd H Weisgraber, Maxim Shusteff, Joshua DeOtte, Eric B Duoss, Joshua D Kuntz, Monika M Biener, Qi Ge, Julie A Jackson, Sergei O Kucheyev, Nicholas X Fang, and Christopher M Spadaccini. Ultralight, Ultrastiff Mechanical Metamaterials. 344(6190):1373–1376, June 2014.

[62] L. R. Meza, S. Das, and J. R. Greer. Strong, lightweight, and recoverable three-dimensional ceramic nanolattices. *Science*, 345(6202):1322–1326, September 2014.

[63] Huachen Cui, Ryan Hensleigh, Hongshun Chen, and Xiaoyu Zheng. Additive Manufacturing and size-dependent mechanical properties of three-dimensional microarchitected, high-temperature ceramic metamaterials. *Journal of Materials Research*, 33(3):360–371, February 2018.